s

# ~~A Numerical Investigation~~ Proof of Concept for Multirotor Systems with Vortex-Generating Modes for Regenerative Wind Energy: ~~Validation Against~~ A Study Based on Numerical Simulations and Experimental Data

Flavio Avila Correia Martins[1], Alexander van Zuijlen[1,‡], and Carlos Simão Ferreira[1]

[1]Faculty of Aerospace Engineering, Flow Physics and Technology Department, Wind Energy Section ([‡]Aerodynamics Section). Delft University of Technology, Kluyverweg 1, Delft, The Netherlands

**Correspondence:** Flavio Avila Correia Martins (f.m.martins@tudelft.nl)

**Abstract.** ~~The current work describes and assesses multirotor systems consisting of pared multirotor and rotor-sized wings, dubbed atmospheric boundary layer~~ This study investigates the potential of regenerative wind farming using multirotor systems equipped with paired multirotor-sized wings, termed Atmospheric Boundary Layer (ABL) ~~control devices, in the rotor's near wake region . The~~ control devices, positioned in the near-wake region of the multirotor. These ABL-control devices ~~create~~ generate vortical flow structures that ~~can accelerate the~~ enhance vertical momentum flux from the flow above the wind farm into the wind farm flow, ~~thus augmenting the wake-recovery process. Understanding the wake-wide impacts of this novel ABL-controlling strategy is crucial to determining the feasibility of using such a strategy in utility-scale wind farms. This work provides~~ thereby accelerating the wake recovery process. This work presents numerical assessments of a single multirotor system ~~accompanied by different ABL-controlling setups~~equipped with various ABL-control configurations. The wind flow is modeled ~~via~~ using steady-state ~~Reynolds-averaged Navier–Stokes computations. The multirotor and ABL-controlling devices are modeled using~~ Reynolds-Averaged Navier-Stokes (RANS) computations, with the multirotor and ABL-control devices represented by three-dimensional actuator surface models based on ~~the~~ Momentum theory. ~~Input force~~ Force coefficient data for the actuator surface models~~and~~ , as well as validation data for the numerical computations~~were measured~~ , were obtained from a scaled model at TU Delft's Open Jet facility. The performance of the ~~ABL-controlling devices was assessed via~~ ABL-control devices was evaluated by analyzing the net momentum entrained from the flow above the wind farm ~~flow~~ and the total pressure and power available in the wake. ~~It was found thatwhen the ABL-controlling strategy is adopted, the~~ The results indicate that, when the ABL-control strategy is employed, vertical momentum flux ~~becomes the primary~~ may become the dominant mechanism for wake recovery~~such that for~~ . In configurations with two or four ~~ABL-controlling~~ ABL-control wings, the total wind power in the wake recovers to 95% of the free-stream value at ~~locations~~ positions as early as $x/D \approx 6$ ~~downwind of a~~ downstream of the multirotor system, ~~which is about one~~ representing a recovery rate approximately an order of magnitude faster than ~~what is seen for~~ that observed in the baseline wake without ~~ABL-controlling capabilities.~~ ABL-control capabilities. It should be noted, however, that this study employs a simplified numerical setup to provide a proof of concept, and the current findings are not yet directly applicable to real-world scenarios.

## 1 Introduction

Our energy transition goals require a ~~significant~~ substantial increase in installed wind power capacity, which is typically achieved by expanding the number and size of wind farms. However, scaling up wind farms ~~, both onshore and offshore , presents~~ — whether onshore or offshore — introduces various challenges, including technical, environmental, economic, and social acceptance issues. For ~~example~~instance, large onshore wind farms can ~~create~~ lead to conflicts with nearby ~~residents~~ communities due to noise and visual ~~pollution~~impact concerns (**??**). ~~Likewise~~Similarly, large offshore wind farms often ~~face~~ encounter high operational and energy transmission costs (**?**). To address the ~~need~~ demand for larger wind farm areas, ~~we can~~ it is crucial to improve the ratio of total power output per ~~land~~ unit of land or sea surface area by enhancing the wake-recovery process. ~~In this study , we evaluate~~ This study evaluates multiple configurations of a novel ~~atmospheric boundary layer~~ Atmospheric Boundary Layer (ABL) control strategy (**?**) ~~that boosts~~ which enhances vertical momentum flux ~~in~~ within a wind farm, thereby increasing the total power output per ~~land surface~~ unit area.

The need for larger wind farms is ~~closely~~ intrinsically linked to the spacing required ~~for effective wake recovery between consecutive~~ to ensure effective wind energy recovery between successive wind turbines (~~see~~ refer to the top diagram in Fig. 1). ~~With~~ Given that the characteristic height of the ABL ~~around~~ typically extends to approximately one kilometer, wind farms ~~covering a surface area of over 1020 km~~ spanning areas of 10-20 km or more can approach the asymptotic limit of "infinite~~" "~~ wind farms. In this ~~scenario~~regime, the boundary layer flow may ~~reach~~ achieve a fully developed state, ~~where most kinetic energy entrainment occurs~~ wherein the majority of kinetic energy must be entrained from above the farm (**?**). ~~In such cases, velocity fluctuations become the primary source of kinetic energy. Since momentum transfer via velocity fluctuations is typically slow, there is a clear need for better strategies to accelerate wake recovery~~As turbulent mixing under these conditions is inefficient in transferring momentum from the flow above the farm to the wind farm flow, improved strategies for optimizing wind farm power output are required. The most ~~common strategies can generally be categorized into three types~~prevalent strategies for this purpose can be broadly categorized into two strategies: i. ~~wing-pitch control, ii. yaw control, and iii. torque controlstrategies~~*thrust vectoring* and ii. *thrust magnitude* control.

~~The central concept of wing-pitch control strategies is to steer the wake~~ Thrust vectoring strategies aim to introduce cross-flow momentum, steering the wake of upstream turbines away from downwind turbines ~~(?). Wake recovery via blade-pitch control is a well-explored topic in the literature, commonly based on blade-element-momentum theory for rotor aerodynamics (?) . ? examined how typical H- and W-type~~ . Numerous studies have focused on improving wind farm power output through *yaw-control strategies* for thrust vectoring (**?**). According to Newton's third law, the thrust exerted by a turbine on the wind generates an equal and opposite reaction force. Thus, if an upstream turbine is yawed positively, the wake will skew negatively, and vice versa. Research on yaw control for wake steering has been ongoing for at least two decades, with significant advancements in the last ten years, particularly for horizontal-axis wind turbines (HAWTs) (**?**). Various methods have been explored to optimize yaw angle controllers (**??**). For instance, **?** reported a 1.4% increase in energy yield in their simulations compared to a baseline case, while **?** found improvements of up to 3.24% using a variable yaw-control strategy. In vertical-axis wind ~~turbines~~ turbine (VAWT) ~~generate two~~ farms, wake deflection is typically achieved by modifying the rotor blade

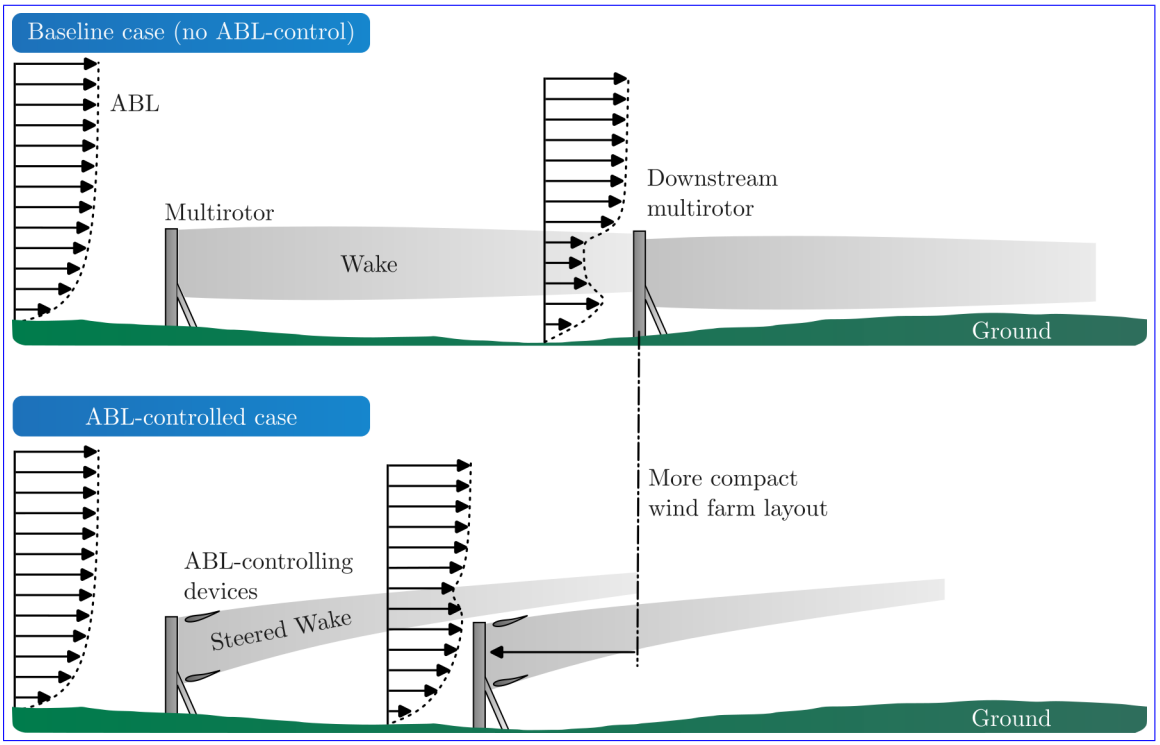


**Figure 1.** The figure ~~shows~~ provides a schematic ~~illustration~~ representation of the wake ~~behind~~ generated by a multirotor system, shown before (top) and after (bottom) ~~implementing ABL-control~~ the implementation of ABL control systems. ~~By directing~~ The ABL control directs the wake upward into the atmosphere, enhancing vertical momentum flux and accelerating wake recovery. This mechanism allows ABL-controlled wind farms ~~can~~ to achieve higher power output per unit of land or sea area, ~~allowing them to be~~ facilitating a more compact wind farm design.

configuration to introduce momentum transfer driven by vorticity into the wake. For example, **?** reported a 13.1% increase in energy yield compared to a baseline case when implementing active pitch control in their VAWT experiments.

Thrust vectoring can also be achieved via *blade-pitch control* strategies, which aim to manipulate a turbine's induction factor by dynamically adjusting its operating point to steer the wake (**?**). Wake recovery through blade-pitch control has gained attention more recently. For example, **?** explored how pitched H- and W-type VAWTs generate two counter-rotating ~~tip vortices at the ends of the blades, which sustain more accelerated wake deflection in comparison with non-pitched wings (???) . Ferreira proposed that by shifting the VAWT's pitching axis (along the blade's quarter-chord length), additional cross-wind momentum could be added to the incoming streamlines, thereby speeding up wakedeflection. His work has inspired similar numerical and experimental research on VAWT wake deflection via pitched blades. ? investigated~~ tip vortices at the blade ends, enhancing wake deflection compared to non-pitched blades (**???**). Similarly, **?** examined the topologies of wakes deflected by pitched VAWTs using actuator line models with unsteady Reynolds-averaged Navier-Stokes (RANS) simulations. ~~Jadeja noted that the~~ , finding that wake-deflection ~~strategy~~ strategies via VAWT blade pitching ~~has the advantage of not affecting the upstream turbine's performance~~ do not compromise the performance of upstream turbines, unlike yaw control strategies~~used~~

for horizontal-axis wind turbines. . Additionally, **?** measured wake deflections of an H-shaped VAWT at different pitching anglesand observed various pitching angles, demonstrating that blade-tip vortices could effectively double the rate of lateral wake deflection through active pitch control.

Many studies also focus on improving wind farm power output through yaw-control strategies (**?**). In VAWT farms, wake deflection is usually achieved by altering the rotor blade layout to generate momentum-carrying vorticity in the wake (**?**). Yaw and blade-pitch control strategies can also be combined. For instance, **?** found that adjusting blade pitch can mitigate the excess loads induced by yaw control. Lastly, torque control strategies aim to manage the strength of the turbine wake to increase *Thrust magnitude control* strategies aim to mitigate power losses by accelerating wake recovery. A common approach within this framework is *axial induction control*, where the goal is to modulate the wake strength of upstream turbines to enhance overall wind farm power production. This approach reduces strategy involves reducing the induction factor of upstream turbines in exchange to increase the kinetic energy available for to downstream turbines (**?**).

However, the wake-recovery Most research on axial induction control relies on low-fidelity simulations and analytical models that approximate wake-turbine and wake-wake interactions, yielding promising results (**??**). However, as noted by **?**, power gains observed in experimental implementations of axial induction control have been relatively modest.

Innovative thrust magnitude control strategies such as Pulse (**?**) and Helix (**?**) have also been investigated. The Pulse method involves rapid, pulsating pitch adjustments to reduce load peaks and manage power output (**?**). Both Pulse and Helix methods disturb the wake through dynamic blade pitching, initiating natural mixing processes closer to the turbines. In the Pulse method, the pitch angle of all rotor blades is varied collectively in a sinusoidal pattern. Conversely, the Helix strategy controls the blade pitch angle individually, with sinusoidal variations and phase offsets between the blades. Simulation studies indicate that these methods can increase the power output of a two-turbine wind farm by up to 5% with the Pulse method and up to 7.5% with the Helix method under turbulent inflow conditions (**?**).

Despite their potential, the wake recovery strategies mentioned above have common shortcomings. They require complex changes share common limitations. They necessitate complex modifications to wind farm control algorithms, which can may conflict with reliability and safety-oriented controls. These strategies can also impose additional loading patterns on conventional turbine designs, potentially leading to premature failures (**?**). Most importantly, they usually Moreover, they typically penalize the performance of individual turbines to enhance wake reenergizing, hoping the downstream turbine' s power gains with the expectation that the downstream turbines' power gains will outweigh the upstream 's losses. Consequentlylosses. As a result, total power production can rarely increase by increases are rarely more than about 30% (**?**) in the best laboratory conditionsunder optimal laboratory conditions (**?**). For example, **??** **?** reported a 5% increase in annual energy production at the Princess Amalia Wind Park in the Netherlands using a combined layout optimization and wake yaw steering control strategy. ThusTherefore, these methodologies may not offer as much have limited potential for reducing wind farm size in real-life real-world scenarios.

This study proposes a new wake-reenergizing strategy that can significantly extend presents a wake-steering strategy aimed at enhancing the energy potential of wind farms. We describe and assess multirotor setups with paired multirotor and , thereby enabling more compact wind farm layouts. We explore the use of multirotor systems equipped with rotor-sized

wings, referred to as ABL-control devices, ~~placed in the near wake~~ which are positioned in the near-wake region (see ~~bottom panel in Fig. 1)~~Fig. ~~In this setup, the~~ 1, bottom panel). These rotor-sized wings ~~create~~ generate vortical structures that ~~accelerate~~ enhance vertical momentum flux from above the ABL into the wind farm, ~~increasing net power production. Note~~ ~~that ABL-controlling systems are intended to consist of~~ thereby allowing for denser turbine configurations. While ABL-control systems are envisioned as comprising multiple multirotor setups ~~combined with ABL-controlling mechanisms. However~~with integrated ABL-control mechanisms, this paper focuses on evaluating the performance of a single multirotor system equipped with ~~ABL-controlling devices. Multirotor~~ ABL-control devices. Both the multirotor and ABL-control devices are modeled using three-dimensional actuator surface models based on Momentum theory (see Fig. ~~2~~).

Steady-state ~~RANS computations performed in~~ Reynolds-Averaged Navier-Stokes (RANS) simulations with a uniform, laminar inlet are performed using `OpenFOAM` ~~are proposed to validate~~ to evaluate this proof-of-concept ~~. The effects of the~~ regenerative wind energy system. It is important to highlight that the study utilizes a simplified numerical setup aimed at demonstrating proof of concept, and thus the findings are not yet directly applicable to real-world scenarios. The impact of induced drag by the ABL-control ~~wing's induced drag are also investigated by comparing~~ wings is assessed by comparing simulation models with and without induced drag, allowing for the isolation of additional wake induction effects resulting from the wings' ~~induced dragforces~~drag. The performance of the ABL-control devices is ~~quantified by the wind farm's~~ evaluated based on the total pressure and ~~vertical momentum flux through the ABL . Experimental observations~~ streamwise momentum flux within the ABL across the wind farm. These numerical results are further supported by experimental data obtained from a scaled multirotor system ~~set up in~~ at TU Delft's Open Jet facility~~complement the present numerical results~~.

This paper is organized as follows. In § 2, it is presented the governing equations, numerical setup, and the description of the assessed test cases. In § 3 results are discussed. § 3.2, delves into the main flow features of the ABL-controlled flows via analyses of the velocity and vorticity fields for different possible ABL device configurations. § 3.3 concerns assessing the performance of the different ABL-devices layouts via analyses of the momentum fluxes and quantifying the total pressure and power available in the wake.

## 2 Methodology

### 2.1 The numerical model

We model the flow around the actuator surfaces using the steady-state ~~RANS~~ Reynolds-Averaged Navier-Stokes (RANS) equations for incompressible, turbulent flows (**?**), defined as follows:

$$\nabla \cdot \overline{\mathbf{u}} = 0 \tag{1}$$

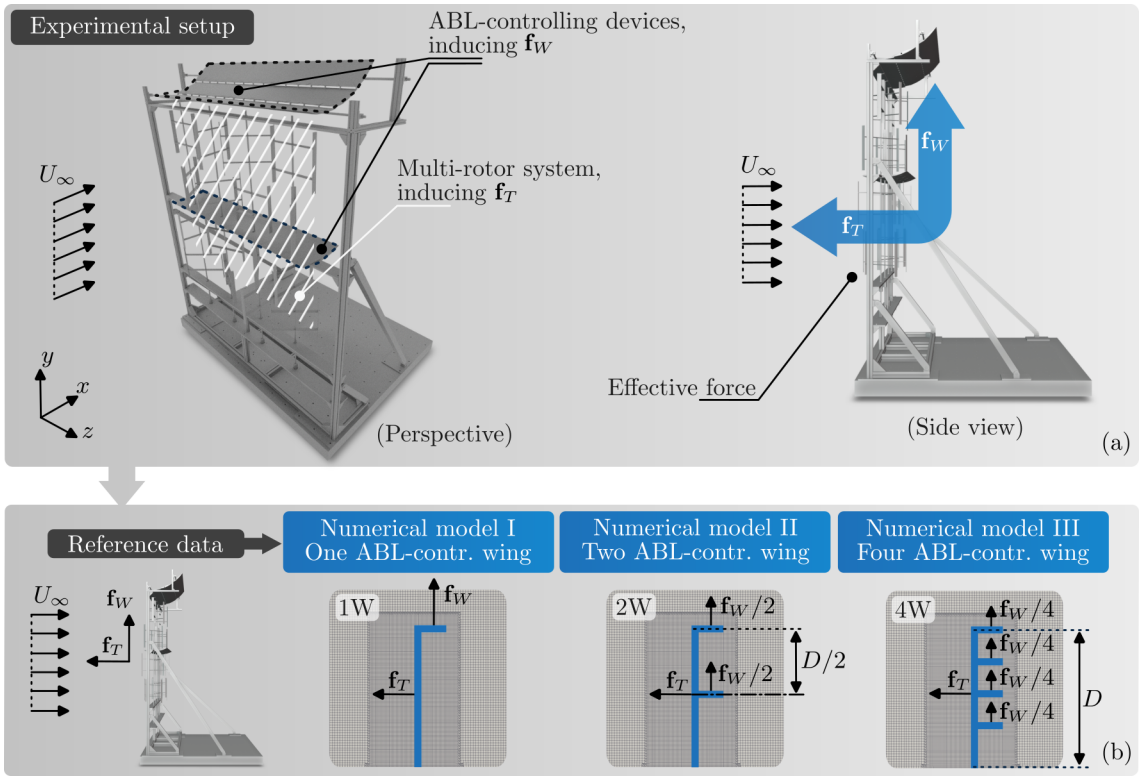


**Figure 2.** Panel (a) ~~shows details~~ provides an overview of the reference experimental setup, while Panel (~~a~~b) ~~in comparison with~~ presents the corresponding numerical model based on momentum theory~~in Panel (b)~~. ~~The experimentally-measured multirotor system's~~ In the experimental setup, the thrust force vector of the multirotor system, $\mathbf{f}_T$, and ~~ABL-system's~~ the effective aerodynamic force of the ABL-control system, $\mathbf{f}_W$, are ~~homogeneously~~ measured. In the numerical model, these forces are distributed homogeneously in a cell-weighted fashion ~~in~~ to replicate the ~~numerical model~~experimental conditions.

$$(\overline{\mathbf{u}}\cdot\nabla)\overline{\mathbf{u}} = -\frac{1}{\rho}\nabla\overline{p} + \nabla\cdot(\nu\nabla\overline{\mathbf{u}}) - \nabla\cdot\mathbf{R} + \frac{1}{\rho}\mathbf{f}_T + \frac{1}{\rho}\mathbf{f}_W, \tag{2}$$

In Eqs. 1 and ~~-~~2, $\mathbf{u} = u_x\hat{\imath} + u_y\hat{\imath} + u_z\hat{k}$ ~~is the velocity~~ represents the velocity vector, $p$ is ~~the~~ pressure, $\rho$ is ~~the density,~~ fluid density, and $\nu$ ~~,~~is the kinematic viscosity~~,~~. The term $\mathbf{R} = \overline{\mathbf{u}'\mathbf{u}'}$ ~~is the Reynolds-stress-tensor, which couples~~ represents the Reynolds stress tensor, coupling the mean flow with ~~the turbulence. The overbar, $\overline{\langle\cdot\rangle}$, and the prime~~turbulence. Here, overbars, $\overline{\langle\cdot\rangle}$, denote time-averaged components, while primes, $\langle\cdot\rangle'$, represent ~~the mean and the fluctuating components of the respective scalar or vector variable. In this study, the homogeneously-distributed force~~ fluctuations.

In this model, $\mathbf{f}_T$ ~~models the effective thrust~~ denotes the homogeneously distributed effective thrust force of the multirotor system, ~~whereas~~ while $\mathbf{f}_W$ ~~models the aerodynamic loads associated with the ABL-controlling wings. Notice that due to constant, homogeneously distributed aerodynamic loadings, the current models are relatively steady, and thus, an~~

~~unsteady models is deemed deferable. Moreover, since the main mechanism for energy transportation relies on the generation and advection of large-scale wing-tip vortical structures, higher-fidelity models~~ represents the aerodynamic forces exerted by the ABL-control wings. These forces are uniformly distributed across the cells of the numerical model, ~~e.g.,~~ simulating a steady-state flow condition. Due to the simplicity of the applied aerodynamic loads, unsteady models are deferred, and higher-fidelity simulations, such as Large-Eddy ~~simulations, are also deemed futile~~ Simulations (LES), are considered unnecessary for this proof-of-concept ~~investigation, where the authors opted for assessing the largest possible number of test cases. As shown~~ study, which aims to maximize the number of analyzed configurations. As discussed in § 3.1, the ~~current steady~~ steady-state RANS model is sufficient for ~~the carried analysis~~this proof-of-concept investigation.

~~The turbulent wind farm flow~~ Turbulent flow within the wind farm is modeled using the shear-stress-transport (SST) $k-\omega$ model (**?**)~~based on an uncertainty assessment conducted~~ , selected based on uncertainty assessments by **?**. The SST model ~~belongs to the linear-eddy-viscosity class of~~ falls within the class of linear-eddy-viscosity RANS models, ~~which assumes a linear relation~~ assuming a linear relationship between Reynolds stresses and the mean strain rate~~(i.e., the~~ , following Boussinesq's hypothesis~~)~~:

$$\mathbf{R} \approx -2\nu_t \overline{\mathbf{S}} + \frac{2}{3}\mathbf{I}k, \tag{3}$$

where $\nu_t$ is the eddy viscosity, $\mathbf{S} = (\nabla\overline{\mathbf{u}} + (\nabla\overline{\mathbf{u}})^T)/2$ ~~,~~is the mean strain-rate tensor, $\mathbf{I}$ is the ~~second-order~~ identity tensor, and ~~$k := \mathrm{tr}(\mathbf{R})/2$~~ $k = \mathrm{tr}(\mathbf{R})/2$ is the turbulent kinetic energy. The eddy viscosity is ~~computed from the turbulent kinetic energy,~~ calculated from $k$ ~~,~~and the specific dissipation rate, $\omega$, ~~which can be estimated using~~ using the following relationships:

$$k = \frac{3}{2}(T_{u,\infty}U_\infty)\frac{3}{2}(T_{k,\infty}U_\infty)^2, \tag{4}$$

~~and~~

$$\omega = \frac{k^{1/2}}{C_\mu^{1/4}D}. \tag{5}$$

~~In the expressions above, $T_{u,\infty}$~~ Here, $T_{k,\infty}$ and $U_\infty$ are the far-field turbulence intensity and ~~reference velocity in the unperturbed, far-field flow, such that $U_\infty := |\overline{\mathbf{u}}_\infty|$; $C_\mu$ is a constant equal to 0.09~~ velocity, respectively, with $U_\infty := \|\overline{\mathbf{u}}_\infty\|$. The constant $C_\mu = 0.09$, and $D$ ~~is~~ represents the reference length scale~~. Here,~~ , which is the side length of the multirotor system ~~is adopted as the reference length scale (see~~ (Fig. 2).

The effects of the multirotor system and ~~ABL-controlling~~ ABL-control wings are modeled as body ~~force~~forces (**?**), ~~such that the effective forces are uniformly distributed~~ distributed uniformly across the finite-volume cells ~~comprising~~ corresponding to

the multirotor and ~~ABL-controlling devices regions, respectively. The distributed multirotor~~ wing regions. The thrust force, $\mathbf{f}_T$, is ~~represented as a source term in~~ incorporated into the momentum equation ~~in~~ (Eq. 2~~, and it is estimated using~~) and calculated as:

$$\mathbf{f}_T = \left(\frac{1}{2}\rho D^2 U_\infty^2\right) C_T \hat{\imath}, \tag{6}$$

where $C_T$ is the ~~effective, experimentally-measured thrust-force coefficient. The ABL-controlling wingsare likewise modeled assource terms in the momentum equation using~~experimentally measured thrust coefficient, and $D^2$ is the projected area of the multirotor system. Similarly, the force exerted by the ABL-control wings, $\mathbf{f}_W$, is represented as:

$$\mathbf{f}_W = \left(\frac{1}{2}\rho A U_\infty^2\right)\left(C_{x,W}\hat{\imath} + C_{y,W}\hat{\imath}\right), \tag{7}$$

where ~~$C_W$~~ $C_W = C_{x,W}\hat{\imath} + C_{y,W}\hat{\imath}$ is the wing's effective force coefficient. ~~The force coefficients~~These force coefficients, $C_T$ and $C_W$, are determined from experimental ~~observations of a scaled model at~~ data obtained from TU Delft's Open Jet Facility (**?**). Further details on the experimental facility can be found on ~~(?)~~the corresponding reference.

### 2.2 Numerical setup

In this ~~work~~study, all numerical ~~computations are performed using~~ simulations were performed using `OpenFOAM` ~~`v9 (??) jointly with the momentum sources , i.e.,`~~ `v9` (**??**), incorporating momentum sources $\mathbf{f}_W$ and $\mathbf{f}_T$, ~~computed using a Momentum-theory-based code written~~ calculated via a Momentum-Theory-based code developed by the authors (**?**). ~~The momentum sources are distributed in a cell-volume weighted fashion onto the cell centers comprising the multi-body systems and~~ These momentum sources were distributed across the computational grid in a cell-volume-weighted manner, centered on the finite-volume cells representing the multirotor systems and the ABL-controlling wings. The multirotor ~~extends one~~ region was modeled as a single finite-volume cell in the streamwise direction~~(i.e., one-cell thick) and is~~, extending $1D$ ~~-long~~ in the spanwise ~~, ($z$-direction)~~ direction. The height of the multirotor ~~system region is~~ region is also $1D$, with ~~its base far $y/D = 0.10$ from the groundplane~~the base located at a distance of $y/D = 0.10$ above the ground. The ABL-controlling wings ~~are also one finite-volume cell wide in the streamwise direction and are~~ were similarly represented as one finite-volume cell thick ~~in the vertical, $y$-directions~~regions with a span of $1D$. The computational domain ~~extends $50D \times 20D \times 10D$ in the downwind,~~ measured $50D \times 20D \times 10D$ in the streamwise ($x$~~, spanwise, ~~), spanwise ($z$), and vertical ~~, ($y$, )~~ directions, respectively~~. The multirotor array is located $10D$ downwind~~ , with the multirotor array positioned $10D$ downstream of the inlet. These domain dimensions satisfy ~~all minimum domain-sizing requirements to minimize the~~ the minimum requirements necessary to mitigate boundary effects on ~~the performance of the turbine (??). Details~~ turbine performance, as outlined by **?** and **?**. A schematic of the numerical setup ~~are shown~~ is provided in Fig. 3.

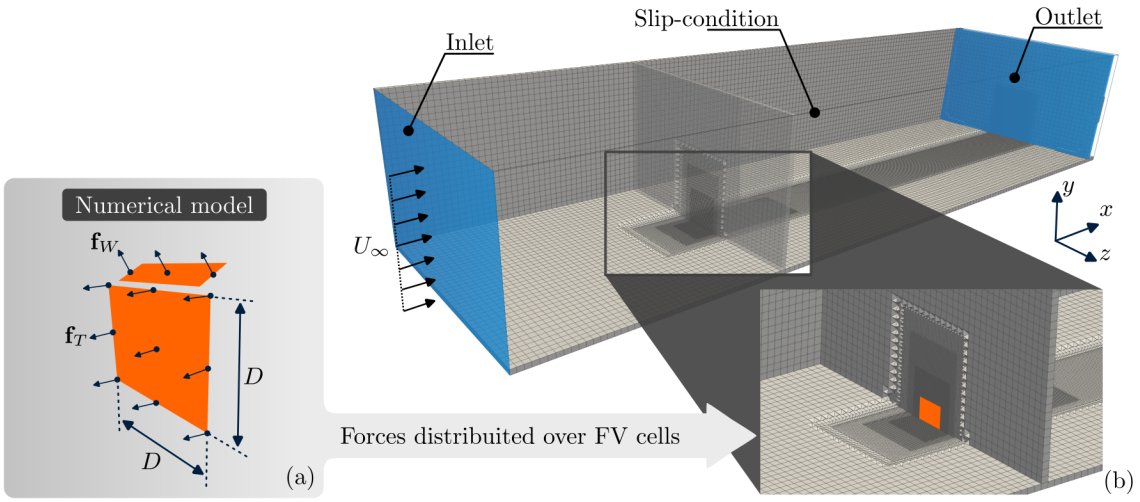


**Figure 3.** Panel (a) shows details of the numerical model based on Momentum theory; panel (b) shows details of the computational domain with the actuator forces modeled as momentum sources. The computational domain is highlighted at the top.

A ~~steady state~~steady-state, incompressible solver~~(i.e., `simpleFoam`) is selected~~, was used for the simulations~~. The SIMPLE method is employed~~, utilizing the SIMPLE algorithm for pressure-velocity coupling. ~~The~~ Gaussian integration was ~~used~~ applied with different interpolation schemes for ~~the spatial discretizationof differential operators. The~~ spatial discretization. Specifically, second-order linear interpolation was employed for gradient terms, ~~the~~ second-order bounded upwind interpolation for divergence terms, and ~~the~~ second-order linear corrected interpolation ~~was employed for the~~ for Laplacian terms. The ~~Geometric~~ pressure field was solved using a geometric agglomerated algebraic multigrid (~~i.e., a~~ V-cycle~~type) solver was adopted with the~~ ) solver with a Gauss-Seidel preconditioner~~method for pressure and its symmetrical version~~, while its symmetric version was used for velocity and turbulence variables. An error tolerance of ~~$1 \times 10^{-6}$~~ $1 \times 10^{-6}$ was adopted for all smooth solvers.

~~Modeling~~ Typically, modeling a neutral ABL involves prescribing inlet boundary conditions ~~providing~~ that provide log-law ~~type ground-normal inflow boundary conditions for wind~~ profiles for velocity and turbulence ~~quantities~~relative to the ground (**?**). However, for this proof-of-concept ~~work, it is deemed more convenient to model the inlet boundary condition with a~~ study, a simplified approach was adopted, applying uniform (Dirichlet) ~~profile for velocity and turbulence-model quantities and~~ profiles for both velocity and turbulence quantities at the inlet, with a zero-gradient (Neumann) boundary condition for pressure. This simplification ~~assumption allows for generalizing the current results by eliminating ambiguousness~~ helps generalize the results by removing complexities associated with ground-normal velocity profiles. The ~~sides of the domain are modeled as a slip (Neumann) boundary condition. The outlet is modeled as a free-stream flow condition and a zero-pressure boundary condition for pressure. The domain's inlet, top ,~~ top and side boundaries ~~are modeled with~~ of the domain were assigned no-slip (Dirichlet) ~~inlet~~ boundary conditions for velocity, pressure, and ~~turbulence-model quantities. The bottom surface of the domain is~~ turbulence variables, while the outlet boundary was modeled as a free-stream condition with zero-gradient pressure. The

bottom boundary employed a slip (Neumann) ~~boundary condition for the~~ condition for velocity and turbulence ~~variables and zero-gradient for pressure. The outlet is modeled as a free-stream flow condition and~~ quantities, with a zero-gradient condition for pressure.

The free-stream ~~wind velocity, $U_\infty$, renders a diameter-based Reynolds number of $Re_D := \rho D U_\infty \mu^{-1}$, of $Re_D \sim 4 \times 10^8$~~velocity, $U_\infty$, corresponds to a Reynolds number based on the multirotor side length, $Re_D = DU_\infty/\nu$, of approximately $4 \times 10^8$. Turbulence quantities ~~are computed from~~ were computed assuming a baseline free-stream turbulence intensity ~~level of $T_{u,\infty} = 1\%$, verging upon values of the reference dataset collected in TU DelftOpen Jet facility~~of $T_{k,\infty} = 1\%$. Although this turbulence intensity does not fully replicate typical atmospheric conditions, it is consistent with experimental data obtained from tests conducted at TU Delft's Open Jet Facility. This selection ensures that the multirotor system is evaluated in an idealized environment where blade-tip vortices are minimally influenced by turbulence. It is important to note that if higher turbulence intensity levels were adopted, wake recovery due to turbulent mixing would be more pronounced than in the cases examined in this study.

### 2.3 Cases descriptions

~~Seven setups are investigated in this study . The setups consist of multirotor systemspaired with~~ This study explores seven distinct configurations of wind regenerative systems, each comprising multirotor setups combined with either four, two, one, or no ABL-controlling wings. To ~~isolate the effects of the~~ assess the impact of induced drag from the ABL-system ~~wing's induced drag on the systems' performance, ABL-controlled~~ wings on overall performance, the numerical models are ~~subdivided into twofold: models with or without the wing's induced drag .~~ divided into two categories: those accounting for induced drag and those without it. This distinction is critical, as the induced drag of the wings may intensify the multirotor's wake, potentially outweighing the wake regeneration benefits of the system.

The thrust coefficient ~~for the numerical model was based on an experimental observation for~~ $C_T$ used in the simulations is based on experimental measurements of a scaled multirotor system operating at a tip-speed ratio of 3.1, ~~resulting in~~ yielding an effective thrust coefficient of approximately ~~$C_T = 0.72$. The effective lift force coefficient of the~~ $C_T = 0.72$. The ABL-controlling ~~system amounts to $C_{y,W} = 0.82$. The effective induced drag~~ system is characterized by an effective lift coefficient of ~~the ABL-controlling system is $C_{x,W} = 0.15$~~$C_{y,W} = 0.82$ and an induced drag coefficient of $C_{x,W} = 0.15$. In all test cases, ~~$\mathbf{f}_T$ and $\mathbf{f}_W$~~ the momentum sources $\mathbf{f}_T$ and $\mathbf{f}_W$ are kept constant and ~~are homogeneously distributed among all~~ uniformly distributed among the wings in a ~~cell-weighted fashion , such that $C_{y,W}$ and $C_{x,W}$ are the same throughout all cases.The~~ cell-volume-weighted fashion (refer to the lower panel of Fig. 2). A detailed summary of the cases ~~contemplated in the current study and the corresponding nomenclatureis highlighted~~ investigated, along with their respective nomenclature, is presented in Table 1~~(note that the authors provided complementary test cases in (?))~~. Additional test cases are discussed in detail in **?**.

**Table 1.** ~~Summary~~ The table provides a summary of the relevant operational parameters for the analyzed wind regenerative system configurations. The nomenclature is defined as follows: "$x$W" represents a configuration with $x$ ABL-controlling wings, and "ND" (i.e., "no drag") indicates the absence of induced drag from the ~~analysed systems~~wings.

| Case name | ABL-devices force coefficients $(C_{x,W}\hat{\imath},\ C_{y,W}\hat{\imath})$ | Number of ABL-controlling wings |
|---|---|---|
| Baseline | $(0,\ 0)$ | 0 |
| 1W | $(0.15,\ 0.72)$ | 1 |
| 2W | $(0.15,\ 0.72)$ | 2 |
| 4W | $(0.15,\ 0.72)$ | 4 |
| 1W-ND | $(0,\ 0.72)$ | 1 |
| 2W-ND | $(0,\ 0.72)$ | 2 |
| 4W-ND | $(0,\ 0.72)$ | 4 |

## 3 Results

### 3.1 ~~Grid-independence analysis~~ Grid convergence and computational model validation

The ~~sizing of the cell elements was set~~ cell sizing was optimized to minimize the ~~grid-sizing influence on the~~ effect of grid resolution on total pressure, ~~$p+\overline{\mathbf{u}}^2\rho/2$. Results are considered grid-independent if~~ $p_t$, defined as $p_t = p + \rho\|\mathbf{u}\|^2/2$. Grid convergence was deemed achieved when the total pressure~~sampled at different planes downwind of the turbines is insensitive (less than~~, measured at various planes downstream of the multirotor, exhibited consistency (within 1%~~different) to~~) despite further grid refinements. ~~Grid refinements were performed~~ Successive grid refinements were implemented by halving the ~~diameter of the cell elements, $\Delta l$, between two consecutive grid refinements. From the grid-independence analysis, it was found that a grid with cell sizings of $\Delta l/D \approx 0.03$~~ cell size, $\Delta l$.

Through the grid convergence study, the following cell sizes were found to be sufficient: $\Delta l/D \approx 0.03$ in the near-wake region (~~$4D \times 2D \times 2D$ wide~~ defined as a $4D \times 2D \times 2D$ box centered on the turbine)~~; $\Delta l/D \approx 0.06$~~, $\Delta l/D \approx 0.06$ along the wake~~and, $\Delta l/D \approx 0.27$~~, and $\Delta l/D \approx 0.27$ in the far-field ~~was sufficient for grid-independent results. The resulting computational grid , consisting of $\approx 2.4 \times 10^6$ cells, is schematically illustrated~~ region. This grid configuration produced a computational mesh of approximately $2.4 \times 10^6$ cells, ensuring each blade-tip vortex was resolved by approximately eight finite-volume cells at formation. A schematic representation of the computational grid is provided in Fig. 3.

The grid convergence analysis results are summarized in Table 2, where the "Fine" mesh configuration was adopted for this study. The relative error between consecutive grid refinements was calculated as the normalized error in total wake pressure, $p_t$.

~~Subsequent to the grid-independence~~ Following the grid convergence analysis, the present numerical model ~~is~~ was validated by comparing ~~the model~~ its results to experimental data ~~collected~~ obtained at TU Delft's Open Jet ~~facility at $Re_D \sim 3.8 \times 10^5$. In Figs.~~ Facility, with a Reynolds number of $Re_D \sim 3.8 \times 10^5$. Figures 4 and 5 ~~, the numerical and measured $u_x$-colored wake profilesat $x/D = 1$ (i.e., one diameter~~ present the wake profiles, color-coded by the normalized streamwise velocity ($u_x/U_\infty$) at $x/D = 1$ (one multirotor side length downstream of the multirotor system)~~are shown. The current~~, for both the numerical and

**Table 2.** Results of the ~~grid-independence~~ grid convergence analysis. The "Fine" mesh ~~is adopted in this study~~was selected for the final simulations. The relative error ~~refers to~~ denotes the normalized ~~error~~ difference between two consecutive grid refinements.

| Mesh | Size of smallest grid element $\Delta l/D$ | Number of finite-volume cells | Relative error in total wake pressure, $p_t$ |
|---|---|---|---|
| Coarse | 0.07 | $1.9 \times 10^5$ | - |
| Medium | 0.05 | $5.4 \times 10^5$ | 0.06% |
| Fine | 0.03 | $2.4 \times 10^6$ | 0.03% |
| Dense | 0.02 | $7.6 \times 10^6$ | 0.03% |

experimental setups~~consist of a multirotor system paired with a double ABL-controlling system. One ABL-controlling wing is at $y/D = 1.25$, whereas the second is at $y/D = 0.75$~~. The reference velocity ~~consists of~~ was derived from time-averaged ~~data obtained through~~ Particle Image Velocimetry ~~. Further details~~ (PIV) data. Detailed descriptions of the experimental setup ~~can be read~~ are available in (**?**) and (**?**).

~~Comparison of simulated flow (left-hand side) and experimental flow (right-hand side) behind a disk actuator model and the multirotor setup, respectively (rotor projected area represented by the white-hashed region). The figure displays $u_x$-velocity colored fields at $x/D = 1$. No ABL control was applied. The experimental velocity field was reconstructed from time-averaged PIV data (refer to (**?**) and (**?**)), while the numerical results were obtained in this study through RANS computations.~~

Figure 4 ~~shows the comparison of the $u_x$-colored velocity fields at $x/D = 1$ without the ABL-controlling devices. Notice that the numerical velocity field yields~~ displays a comparison of $(u_x/U_\infty)$ fields at $x/D = 1$ without ABL-control devices. The numerical results demonstrate a uniform induction field, ~~$a$, $a := (U_\infty - u_x(x = 0))/U_\infty$,~~ defined as $a := (U_\infty - u_x(x = 0))/U_\infty$, within the region behind the multirotor ~~'s region (rotor projected area~~ (represented by the white-hashed ~~region)due to~~ area), consistent with the homogeneously distributed thrust coefficient~~based on Momentum theory. The experimental results show, in contrast, velocity fields with local fluctuations due to~~ . In contrast, the experimental results reveal local velocity fluctuations resulting from the discrete nature of the scaled multirotor array~~. The experimental setup comprises a multirotor system with a $4 \times 4$~~ , consisting of a $4 \times 4$ vertical-axis ~~rotors array. Nonetheless, the results shown in the figure uphold the~~ rotor configuration. Despite these differences, the figure demonstrates a strong correlation between the ~~current numerical and the reference experimental data~~numerical and experimental results, underscoring the validity of the numerical model.

~~In Fig.~~

In Figure 5, the validation ~~exercise~~ is extended to ~~account for~~ include the effects of ~~the ABL-controlling~~ ABL-control wings. The ~~test case in Fig. 5 consists of a setup with an actuator wing at the top of the multirotor device ($y/D = 1.1$) and a second actuator wing at the center of the device (i.e., $y/D = 0.75$). The figure also shows the $u_x$ fields at $x/D = 1$. Once again, there is a strong correlation between the~~ setup consist of a multirotor system coupled with a dual ABL control system. In this configuration, one ABL-controlling wing is positioned at $y/D = 1.25$, and the other at $y/D = 0.75$. The $u_x$-velocity fields at $x/D = 1$ are presented for both experimental and numerical results~~, evident from the induction field behind the multirotor system and the size and shape of the two wing-tip vortices at $y/D \approx 1.35$~~. The core of the measured blade-tip vortex is located at $y/D \approx 1.46$, while the simulated vortex core is found at $y/D \approx 1.48$, resulting in a positional error of approximately 1.7%.

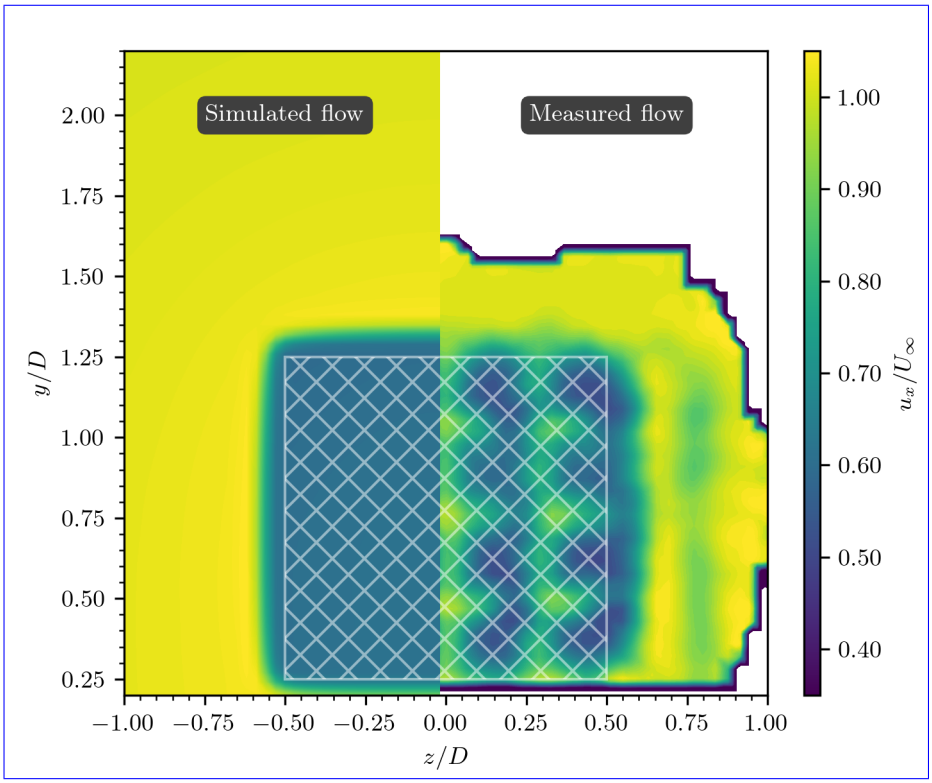


**Figure 4.** Comparison of simulated (left) and experimental (right) flow fields behind a disk actuator model and the multirotor setup, respectively. The white-hashed region denotes the multirotor's projected area. The figure presents $u_x$-velocity colored fields at $x/D = 1$, with no ABL control applied. The experimental velocity field was reconstructed from time-averaged PIV data (see (**?**) and (**?**)), while the numerical results were obtained in this study using RANS computations.

At $x/D = 2$, PIV measurements from (**?**) place the vortex core at $y/D \approx 1.54$, whereas the numerical model predicts a position of $y/D \approx 1.59$, corresponding to a 3.2% error.

### 3.2 ABL-controlled wake characteristics

Figure 6 ~~presents the wake behind the multirotor system as streamwise-velocity colored fields, $u_x/U_\infty$~~illustrates the normalized streamwise velocity fields, $u_x/U_\infty$, at various planes downstream ~~of~~ the multirotor system (with the ~~origin of the coordinate system, i.e., $x/D = 0$~~coordinate origin, $x/D = 0$, at the ~~multirotor's location~~ location of the multirotor system). In all panels, the ~~silhouette of the multirotorsystem is overlaid in white for reference. The~~ white-hashed region denotes the multirotor's projected area, whereas the ABL-controlling devices are ~~represented by the~~ indicated by dotted line segments. The top ~~row illustrates the wake of~~ panels represents the wake for the Baseline case~~without ABL-controlling features. The subsequent rows depict~~ , without ABL-control features, while the subsequent rows show results for increasing numbers of ABL-controlling devices~~,~~. These cases are labeled as 1W-ND '~~ ~~(one wing, no induced drag)~~for one wing~~, 2W-ND '~~ for ~~(two wings, ~~and '~~no

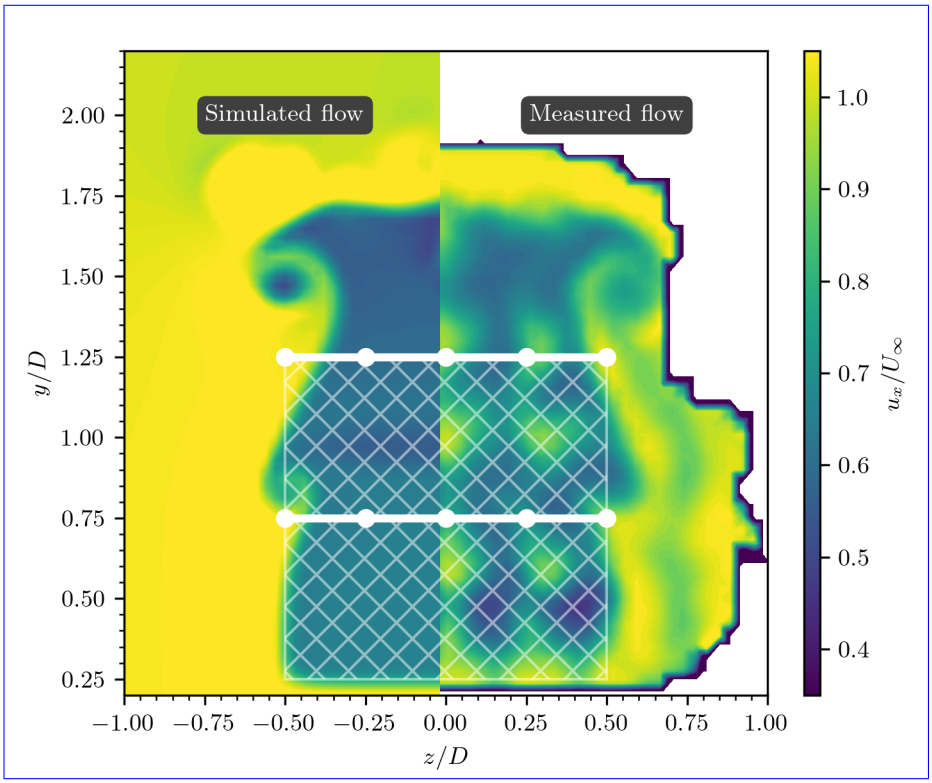


**Figure 5.** Comparison between simulated flows (~~on the left-hand side~~left) and experimental flows (~~on the right-hand side~~right) behind the ABL-controlled setups~~(rotor projected area represented by the~~ . The white-hashed region ~~)~~denotes the multirotor's projected area. The ABL-controlling devices are ~~represented~~ depicted by the dotted line segments. The figure ~~displays $u_x$~~shows $u_x$-velocity ~~colored~~ color fields at ~~$x/D = 1$~~$x/D = 1$. The experimental velocity field was reconstructed from time-averaged PIV data (~~refer to~~see (**?**)), while the numerical results were obtained in this study ~~through~~ using RANS computations. ~~Visual~~ A visual inspection ~~of the figure highlights~~ reveals a strong correlation between the numerical and ~~reference~~ experimental reference results.

induced drag), and 4W-ND ~~' for four wings. The~~ (four wings, no induced drag). The induced drag effects of the ~~wing's induced drag are not considered in these cases~~wings are neglected in these simulations.

~~In cases with ABL-controlling devices, an overall ascent motion with crossflow expansioncharacterizes the general dynamics of the ABL-controlled wakes. Figure 6 also demonstrates that, as expected, the rapid ascent of the wakes is facilitated~~

In the ABL-controlled cases, the wakes exhibit in general an upward motion with lateral expansion, driven by the counter-rotating ~~,~~ wing-tip vortices~~of Cases 1W-ND, 2W-ND, and 4W-ND. Additionally, for Case~~ . For the 1W-ND ~~, fluid~~ case, wake flow parcels near the ~~middle plane $z/D = 0$ are observed to ascend more rapidly compared to~~ midplane ($z/D = 0$) ascend faster than those near the ~~two~~ wing-tip vortices (~~around the $z/D \approx \pm 0.5$ planes~~$z/D = \pm 0.5$), which ~~ascend to the flow~~ reach the region above the turbine (~~$y/D > 1.10$~~$y/D > 1.10$) at lower ~~speeds~~velocities. In the absence of ~~ABL-controlling devices (i.e., the~~ ABL-control (Baseline case), wake ~~re-energizing relies solely~~ recovery depends primarily on momentum exchange ~~via velocity fluctuations on the~~ through velocity fluctuations at the wake's outer shear layers~~of the wake, which is notably~~ , a process significantly less efficient than the wake-steering technique ~~evaluated~~ employed in this study. This ~~observation~~

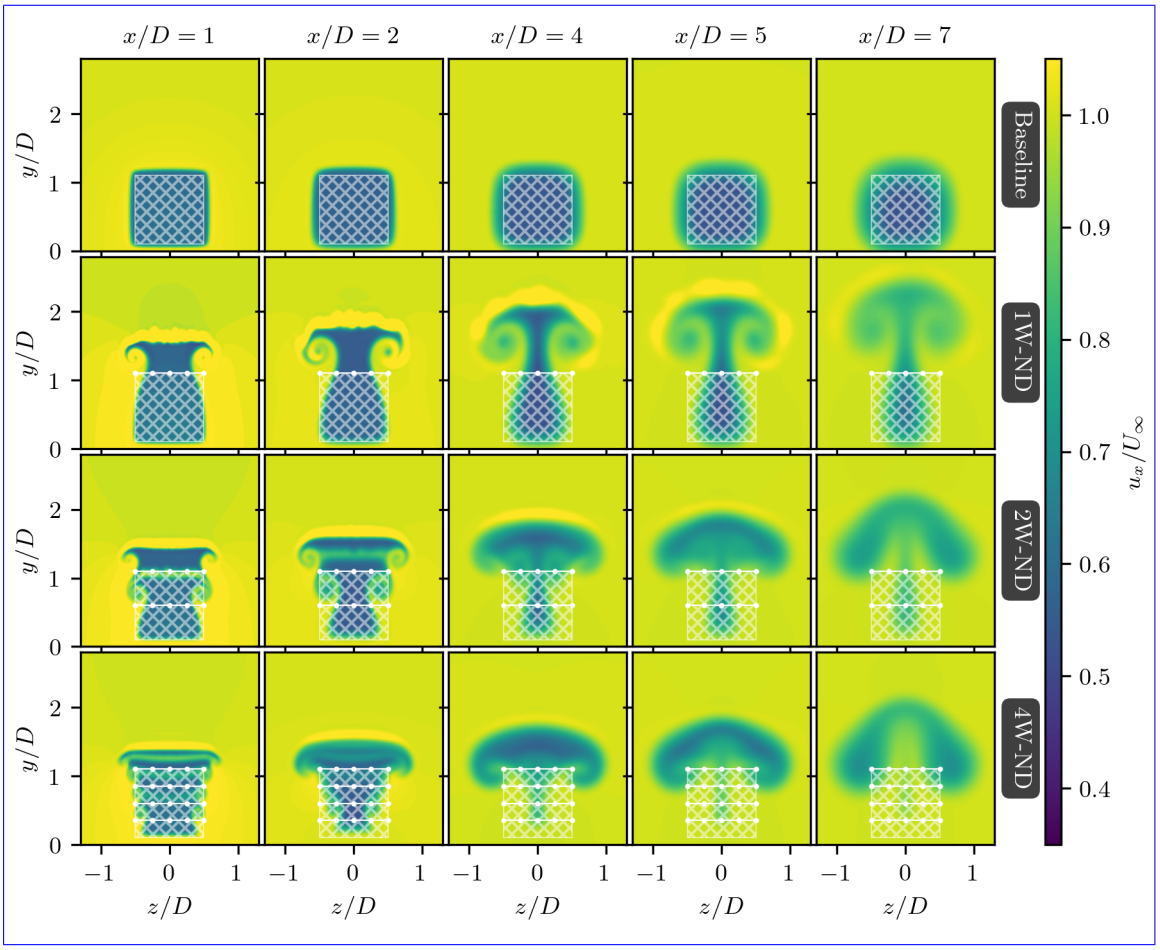


**Figure 6.** Streamwise velocity contours at various downstream locations, $x/D$, behind the multirotor system (with the rotor projected area shown as the white-hashed region). The top row shows the baseline case without ABL-controlling devices, while the subsequent rows present cases with 1, 2, and 4 wings, respectively (wings indicated by white-dotted lines). The effects of the wings' induced drag are excluded from these simulations.

~~is evident from a visual examination of the volume of the~~ can be seen in the larger volume of high-induction flow ~~region that remains at $y/D < 1.10$ for the different cases. Henceforth, we refer to the flow region below the $y/D = 1.10$ plane as the 'wind-farm flow'. The authors also note that these conclusions are applicable to~~ that remains below $y/D = 1.10$ in the Baseline case compared to the ABL-controlled configurations. These conclusions are expected to hold for flows with higher free-stream turbulence ~~intensity levels, provided that large~~ intensities, provided large-scale vortical structures are not dissipated ~~or depleted due to~~ by flow instabilities.

The velocity fields in Fig. 6 ~~indicate~~ demonstrate that the advection of ~~the~~ high-induction fluid parcels ~~behind the multirotor system to~~ into the flow above the ~~wind-farm flow is considerably improved when designs with~~ wake region is significantly enhanced when using two or more wings~~are adopted in comparison with an arrangement with a single wing. The extra efficiency~~

of , as observed in Cases 2W-ND and 4W-NDcompared to Case , compared to the single-wing configuration (1W-NDcan be noted from the visual inspection of the wake 's topology. In ). This increased efficiency is evidenced by the narrower velocity-deficit region in the wake for $x/D > 5$ in Cases 2W-ND and 4W-ND, the velocity-deficit region defining the wake that remains in the wind-farm flow for $x/D > 5$ is substantially narrower compared to what is seen for Case relative to 1W-ND. NonethelessHowever, despite the overall more efficient upwards more effective upward advection of the wake promoted by the extra wings of enabled by the additional wings in Cases 2W-ND and 4W-ND, the velocity-deficit flow is, on average, lower in the ABL in these cases when compared to the results for Case 1-ND. For instance, at the downstream plane $x/D = 7$maximum height of the high-induction flow in these configurations is lower than that observed in Case 1W-ND. For example, at $x/D = 7$, the maximum height of the wake is $y/D \approx 2.6$ for Case reaches $y/D \approx 2.6$ in the 1W-ND , whereas for Cases 2- case, whereas in Cases 2W-ND and 4W-ND, the maximum height of the wake is $y/D \approx 2.2$. The authors remind the reader wake height is limited to $y/D \approx 2.2$. It is important to note that the total vertical force is the same in exerted is identical across all ABL-controlled cases.

The figure shows the streamwise-velocity contours at different downwind locations, $x/D$, behind the multirotor system (rotor projected area represented by the white-hashed region). The top row shows the conventional squared wake of the baseline case without the ABL-controlling devices. Subsequently, the second, third, and fourth rows show results for the ABL-controlled system with 0, 1, 2, and 4 wings (represented by white-dotted line segments), respectively. These simulations do not account for the effects of the wing's induced drag.

Figure 7 extends the results shown in Fig. 6 to account for the Blade's induced drag (see Table 1). The comparison of the setups without (i.e., Cases 1W-ND, 2W-ND and 4W-ND, shown in Fig. 6) against the results with (i.e., Cases 1W, 2W, and 4W, shown in Fig. 7) induced drag reveal that the main flow features of the ABL-controlled systems, such as the vortexes formation, shedding and advection, are not significantly affected by the induced drag. This last conclusion is especially true for the cases with more wings, where the effective drag force is distributed over a larger flow region. For the Case 1W, for which results are shown on the second row of Fig. 7, the concentrated drag force induced on the flow by the single ABL-controlling wing breaks up instabilities over the outer shear layers of the wake. Such instabilities, which originated due to the local curvatures in the induction field behind the drag-inducing wing, are more pronounced on the near-wake region, i.e., at $x/D <\sim 4$, and are quickly diffused under the action of viscosity.

Wind farms with Wake flows incorporating ABL-controlling devices feature exhibit enhanced momentum exchange between the wind farm flow wake flow region and the flow abovethrough , primarily facilitated by wing-tip vortices. Thus, to Note that we refer to the region below $y/D = 1.10$ as the "wake flow region". To fully understand the flow mechanisms promoting the upwards mechanisms responsible for the upward motion of the wake, and more specifically, to understand why the particularly why momentum-deficit fluid parcels are advected upwards at different at varying rates depending on the number of wings and their location across the distinct $z/D$ planes, the visual diagnostics and positioning of the wings across different $z/D$ planes, visual analysis of the velocity fields are alone is insufficient. Instead, assessing the flow through a more comprehensive understanding is gained through an examination of the vorticity fieldsis essential. .

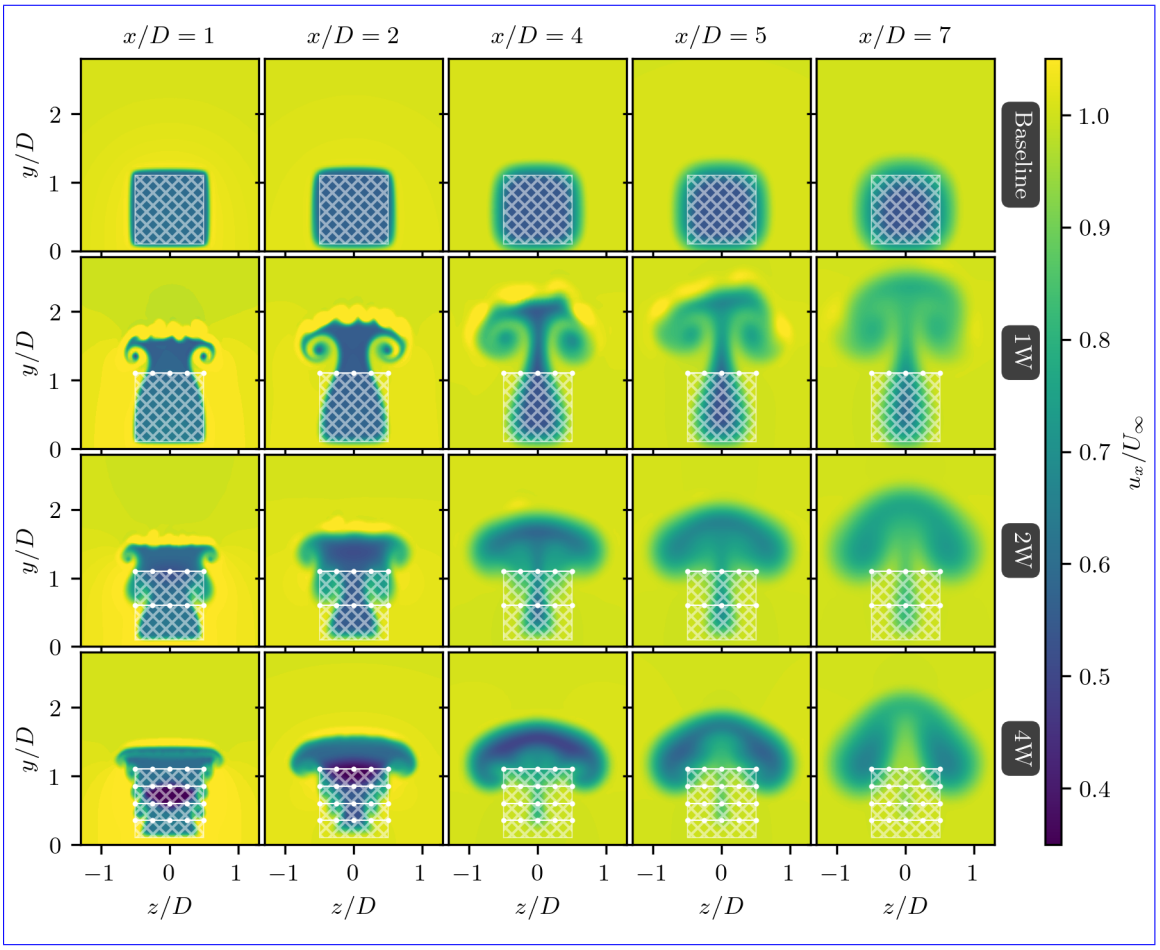


**Figure 7.** This figure extends the results shown in Fig. 6, accounting for the effects of the wing's induced drag. Each panel shows the streamwise-colored wake behind the multirotor system (rotor projected area represented by the white-hashed region) at different downwind locations, $x/D$. Each row shows, from top-to-bottom, results for the ABL-controlled system with 1, 2, and 4 wings, respectively (represented by white-dotted line segments).

Figure 8 ~~shows, top-to-bottom, the downwind-vorticity colored, $\omega_x D/U_\infty$,~~ presents the normalized streamwise vorticity fields, $\omega_x D/U_\infty$, at various cross-sectional planes ~~of the flow for~~ downstream of the ABL-controlled multirotor system, showing the influence of an increasing number of ~~ABL-controlling wings.~~

~~Streamwise-vorticity contours reveal the wing-tip vortexes generated by the different ABL-controlling device designs. Top-to-bottom rows show results for 1, 2, and 4 ABL-controlling wings (represented by black-dotted line segments), respectively.~~

~~Case 1W-ND's~~ wings. Figure 8 compares the vorticity-colored ~~fields, shown in the top row of Fig. 8, reveal the two counter-rotating wing-tip vortices developed behind the multirotorsystem by the single~~ wakes at $x/D = 1, 2, 4, 5,$ and 7 for cases involving varying numbers of ABL-controlling ~~wing. These two~~ wings. To facilitate analysis, both cases with and without the effect of wing-induced drag are displayed, while the baseline case without wings is omitted. The dark-gray hatched region

denotes the projected area of the multirotor, and black-dotted lines represent the wings. In the 1W-ND case (top row), the vorticity fields reveal two counter-rotating wing-tip vortices, which are advected upwards~~and cause the upward motion of wake the closer the flow parcels are to~~. This causes upward displacement of the wake towards the symmetry plane ~~of the flow, $z/D = 0$, while simultaneously inducing the downwash motion of~~ ($z/D = 0$) while inducing downwash in the high-momentum flow above the ~~wind-farm flow at $|z/D| > 0.5$. For Cases~~ wake flow region at $|z/D| > 0.5$. For 2W-ND and 4W-ND ~~, an average upward movement~~ cases, a similar upward displacement of the wake is ~~also observed. However, the mechanisms of the upward flow advection are considerably different in Cases 2W-ND and 4W-ND compared to Case~~ observed, though the driving mechanisms behind this advection differ significantly from the 1W-ND ~~and require an orderly analysisof the events~~case, warranting further analysis.

~~To better understand~~

To further dissect the ABL-controlled flow ~~of Cases~~ dynamics in the 2W-ND and 4W-ND ~~, let us first subdivide the advection of the wake in Cases 2W-ND and 4W-ND into threefold based on the steps of the upwards-motion mechanisms~~cases, the wake advection process is subdivided into three distinct stages: i. ~~$x/D \in \sim [0,2]$~~vortex formation ($x/D \sim [0,2]$), ii. ~~$x/D \in \sim [2,5]$ and iii. $x/D \in \sim [5,\infty[$. The authors will denote here, for simplicity, step i. as "vortex-formation"; step ii. as "vortex-coalescing"~~ vortex coalescence ($x/D \sim [2,5]$), and iii. ~~as "vortex-advection" step. During the vortex-formation step, the~~ vortex advection ($x/D \sim [5,\infty[$). These stages capture the progressive mechanisms of wake displacement.

During the vortex formation stage, wing-tip ~~vortex is advected~~ vortices are carried downstream by the mean flow. ~~Concomitantly, the vortices that are~~ Simultaneously, vortices above the barycenter of the vortical system (~~i.e.,~~ the horizontal line equally ~~apportioning the vortices above it with the vorticesbelow it~~dividing the vortices) are pushed ~~outwards~~ outward from the symmetry plane~~$z/D = 0$ (see Fig. 8), whereas the vortices below the barycenter of the vortical system are pushed inwards, i.e., towards the plane $z/D = 0$. Notice also that these lateral motions of the vortical system are~~ , while those below are drawn inward toward it. This lateral self-induced ~~. During the vortex-coalescing process~~motion is visible at $x/D = 2$ in the 2W-ND and 4W-ND cases (Fig. 8).

In the vortex coalescence stage, the low-pressure ~~regions correspondent to the core~~ cores of the wing-tip vortices ~~act as attracting regions, and the multiple wing-tip vortices coalesce~~ serve as attractors, leading to the merging of vortices into two skewed ~~,~~ counter-rotating ~~vortical structures(see corresponding panels for $x/D = 4$ in Fig. 8). In the third and last step, i.e.~~ structures, ~~for $x/D > 5$, the~~ as observed at $x/D = 4$. Finally, in the vortex advection stage ($x/D > 5$), the mutual induction fields of ~~one vortice on another mutually propel the two vortical systems upwards~~ these vortices propel the paired structures upward into the atmosphere. ~~Notice that for~~ Notably, in Case 1W-ND, ~~this third step co-occurs with the vortex formationprocess, thus explaining why the upwards-advection~~ vortex advection occurs concurrently with vortex formation, which explains the more rapid upward advection of the vortex ~~paired in Case 1W-ND takes significantly less time to move to the flow above the wind farm flow, as observed from~~ pair compared to the other cases, as previously seen in Fig. 7.

~~Figure 8 includes vorticity fields of setups accounting for the ABL-controlling devices's induced drag , i.e., Cases~~ Additionally, Fig. 8 presents the vorticity fields for cases including the effects of wing-induced drag (1W, 2W, and 4W~~. The comparison of the streamwise vorticity fields for the cases~~ ). A comparison between setups with and without ~~the effects of induced drag~~

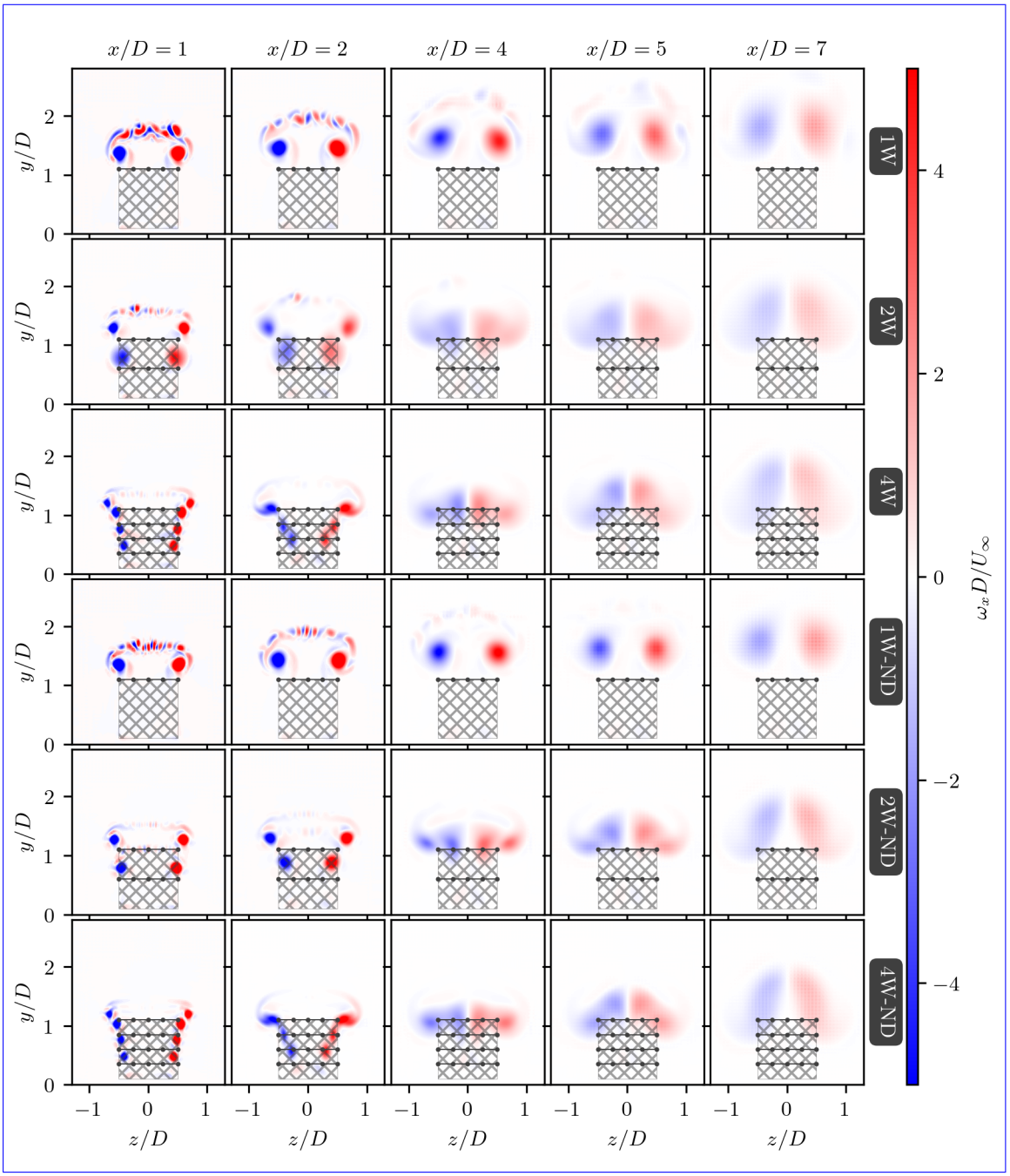


**Figure 8.** Streamwise vorticity contours highlighting the wing-tip vortices generated by different ABL-controlling configurations. Top-to-bottom rows represent results for 1, 2, and 4 ABL-controlling wings (depicted as black-dotted line segments), respectively.

~~reveals~~ induced drag shows that, despite the ~~considerable magnitude of $C_{x,W}$, the~~ substantial contribution of $C_{x,W}$, the overall dynamics of the wing-tip vortices ~~are relatively unaltered in the presence of the induced drag effects. Nonetheless, it is evident~~

that when drag forces are accounted for, a surplus of flow instabilities is introduced over the topmost region remain largely unaffected. However, drag forces introduce flow instabilities in the upper regions of the wake. Such three-dimensionalities are naturally associated with turbulent mixing that can ultimately contribute to the mixing between the wind farm flow , which are associated with increased turbulent mixing. These three-dimensional instabilities may enhance interactions between the wake-flow region and the flow abovethe wind farm.

Given that the wing-tip vortices are serve as the primary mechanism for moving the transporting low-momentum flow of the wake upwards in exchange for moving the wake flow upward while simultaneously drawing high-momentum ABL flow downwardsdownward, a simplified analysis of the flow in the view of these vortices using the Kutta-Joukowski theorem is deemed relevant. Let us denote Denoting the circulation around a closed contour in an arbitrary crossflow plane , $yz$, by $\Gamma_x$. If the conservative-flow assumption is adopted$(yz)$ by $\Gamma_x$, and assuming a conservative flow, the Kutta-Joukowski theorem expresses that allows us to approximate the circulation associated with the wing-tip vortices of in Case 1W (or 1W-ND) can be approximated byas:

$$\Gamma_x = -C_y U_\infty \frac{D}{2}. \tag{8}$$

MoreoverFrom potential flow theory, it is also known from potential flow theory known that the tangential velocity $u_\theta$ $u_\theta$ induced by a point-vortex idealization at a flow parcel distant $r$ from the same point-vortex is $u_\theta = -\Gamma_x/2\pi r$. Thus, if we approximate the current flows to point vortex at a distance $r$ from the vortex center is given by $u_\theta = -\Gamma_x/2\pi r$. Under the assumption of a conservative flowidealization, it is straightforward , it follows that the vertical velocity $u_y \approx u_y(z/D)$ $u_y$, induced at the symmetry plane $z/D = 0$ of the flow, $u_y(z/D = 0)$, due to $z/D = 0$ by the two wing-tip vortices for of a single ABL-controlling wingis , is approximately:

$$u_y(z/D = 0) \sim 2u_\theta \sim \frac{C_y U_\infty}{\pi}\hat{\imath}. \tag{9}$$

The result above shows that due to the action of the wing-tip vortices, fast This result indicates that the upward advection of fluid parcels that scale with $U_\infty$ is expected near the $z/D = 0$ plane . Contrastinglyscales with $U_\infty$ near the $z/D = 0$ plane due to the action of the wing-tip vortices. By contrast, the vertical velocity induced on by one wing-tip vortex by anotherscaled with the distance $D$ is, thus, similar to $u_y(z/D = \pm 1/2) \sim C_y U_\infty/4\pi\hat{\imath}$, i.e.on another, scaled by the distance $D$, is $u_y(z = \pm D/2) \sim C_y U_\infty/4\pi\hat{\imath}$, leading to the ratio:

$$\frac{u_y(z/D = 0)}{u_y(z/D = \pm 1/2)} \frac{u_y(z = 0)}{u_y(z = \pm D/2)} \sim 4. \tag{10}$$

The ~~results~~ result in Eq. 10 ~~explain why the flow parcels $z/D = 0$ are advected upstream at considerably quicker rates than the flow parcels in close proximity~~ explains why wake flow parcels near $z/D = 0$ are advected upward more rapidly than those closer to the vortical structures themselves. ~~Figure~~This behavior is confirmed in Fig. 9, ~~showing the $u_y$-velocity colored flows past~~ which shows $u_y$-colored velocity fields at $x/D = 7$ for various ABL-controlled wakes~~at $x/D = 7$, confirms the analytical results deduced above. The panels in the figure show, left to right, ~~. The figure presents results for Cases 1W, 2W, and 4W , respectively. Results for Cases (left to right), while results for the non-drag cases (1W-ND, 2W-ND, and 4W-ND~~are similar and ~~)~~ are omitted for ~~conciseness~~brevity, as they exhibit similar behavior.

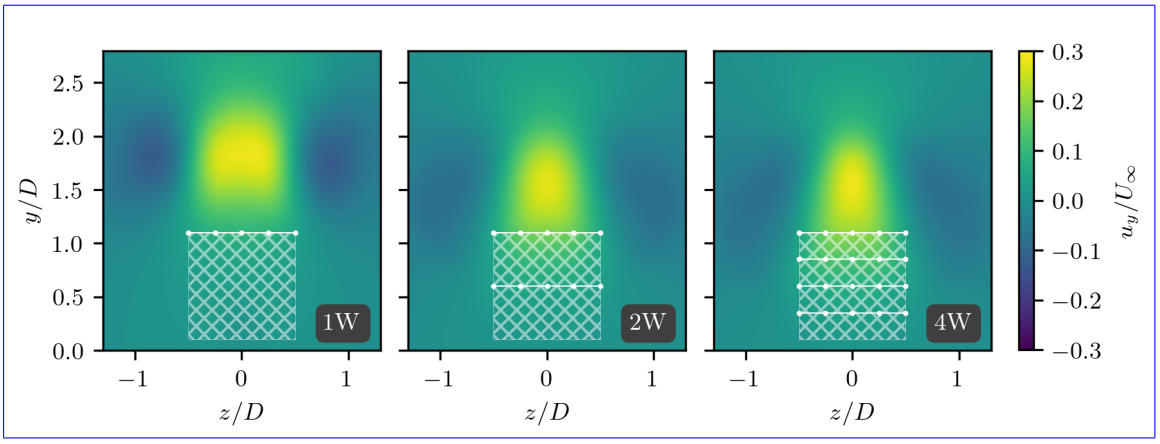


**Figure 9.** ~~Wakes of~~ Vertical velocity $u_y/U_\infty$ in ABL-controlled setups~~, colored b $u_y/U_\infty$ (~~. The white-hatched region represents the rotor's projected area~~represented by the white-hashed region~~, and the white-dotted lines depict the ABL-controlling devices~~represented by white-dotted line segments~~)~~. This figure ~~illustrates~~ confirms the ~~outcomes~~ behavior described by Eq. 10, ~~where $u_y$ is at its~~ showing maximum $u_y$ at the ~~$z/D = 0$~~ $z/D = 0$ plane.

~~Let us extend the above analysis to configurations with multiple wings, specifically Cases 2W and 4W. From~~ As previously mentioned, the visual inspection of the velocity and vorticity fields ~~above (see~~ (Figs. 7 and 8) ~~, it was concluded that~~ suggests that setups with more wings enhance the advection of low-momentum fluid parcels ~~is more efficient in setups with a greater number of wings. This assertion is revisited~~ compared to the setup with a single wing. Re-examining this in light of potential flow theory~~:~~ , the circulation associated with each wing-tip vortex, ~~$\Gamma_x$, causes the~~ $\Gamma_x$, causes vortices generated by wings at lower heights to push those ~~formed by the higher wings~~ at higher locations outward. Simultaneously, vortices at higher ~~$y/D$ locations push the vortices beneath them inward , toward the $z/D = 0$ plane. This trend~~ $y/D$ locations exert an inward influence on those below. This phenomenon is evident from the relative positions of the vortex cores ~~relative to the~~ $y$along the $y$-axis ~~on the $x/D = 2$ panels for~~ in the $x/D = 2$ panels of Cases 2W and 4W ~~in~~ (Fig. 8~~. During the vortex-coalescence step, the~~ ).

During the vortex coalescence stage, the low-pressure cores of the wing-tip vortices act as centers of attraction, promoting the merging of multiple vortices into two counter-rotating structures. The induced velocity fields ~~resulting from~~ generated by the circulation of the ~~top-most vortices facilitate~~ topmost vortices aid the upward advection of the ~~bottom-most vortices. This process is~~ lower vortices, driven by the ~~underlying pressure field, promoting vortex coalescence. As the coalescenceleads~~

~~to the formation of two counter-rotating vortices, their induction fields further enhance their mutual upward advection. This coalescence and advection occur around $x/D = 4$ in~~ pressure field. This coalescence, followed by upward advection, occurs around $x/D = 4$ (Fig. 8). Consequently, ~~only around $x/D \approx 4$ do~~ at approximately $x/D = 4$, the low-momentum fluid parcels ~~, swirling~~ trapped within the vortices ~~,~~ encounter favorable conditions ~~to ascend to~~ for upward movement into the higher regions of the ABL. The requirement for ~~the formation of these large vortices before the entire wake can be advected upward~~ vortex formation and coalescence before efficient wake advection explains why systems with more wings are slower at elevating the wing-tip vortices, despite being more efficient at transporting low-momentum flow upwards~~, while simultaneously being slower at elevating the wing-tip vortices.~~

~~Schematic diagram illustrating the mechanisms promoting the upward advection in the wake. Setups with a single wing behind the multirotor system (represented as green line segments) move the wing-tip vortexes farther up the atmosphere. In contrast, setups with more wings advect the wing-tip vortices upwards more slowly but are more efficient in moving more low-momentum flows upwards.~~.

From this analysis, the most significant distinction among the examined ABL-control configurations emerges when categorizing them into two groups: single-wing setups and those with multiple wings. Figure 10 ~~includes~~ presents a schematic diagram ~~of the processes taking place in each ABL-controlling strategy discussed above. The~~ illustrating the momentum transfer mechanisms ~~are divided here into twofold: setups with a single ABL-controlling wing and configurations with multiple wings. This subdivision is based on the current results, which suggest that the mechanics of the ABL-controlling systems can generally be classified into these two categories~~observed in these two types of configurations. In the diagram, arrow thickness ~~indicates the intensity (i.e., magnitude) of the underlying velocity field~~ represents velocity field intensity, while vortex cores are depicted as spirals. ~~The flow evolution is represented~~ Flow evolution is illustrated in three stages~~for both cases~~, progressing from left to right for both configuration types.

### 3.3 Momentum entrainment

In the previous subsection, the ~~topology of the wakes of the~~ wake topology of ABL-controlled systems was ~~analysed using the~~ analyzed using velocity and vorticity fields. This subsection focuses on the momentum and energy balances ~~of~~ within the ABL-controlled flows for the different design strategies ~~of~~ considered in Cases 1W, 2W, 4W, 1W-ND, 2W-ND, and 4W-ND.

In the RANS framework, the momentum flux across a differential surface element $dS$ enclosing the wake behind the multirotor system is given by $(\rho\overline{\mathbf{u}} \cdot d\boldsymbol{S})\overline{\mathbf{u}}$. In the finite volume approach, this expression is approximated as $(\rho\overline{\mathbf{u}}_j \cdot \boldsymbol{S}_j)\overline{\mathbf{u}}_j$, where $j$ denotes the index of the finite-volume cells that form the surface $S$ in the computational fluid dynamics (CFD) mesh, and $\boldsymbol{S}_j$ represents the surface area vector of the cell. Considering that the computational mesh is composed of planes with uniform cell sizes, $\Delta l$, and the cells are represented by cubic finite-volume elements, the surface area vector can be expressed as $\boldsymbol{S}_j = \Delta l\hat{i} + \Delta l\hat{j} + \Delta l\hat{k}$. Under this assumption, the momentum transferred across the $j$-th cell is $(\rho\Delta l)u_{x,j}\overline{\mathbf{u}}_j$ for the $y$-normal (horizontal) plane, and $(\rho\Delta l)u_{z,j}\overline{\mathbf{u}}_j$ for the $z$-normal (vertical) plane. Therefore, the streamwise momentum transferred across these planes is $(\rho\Delta l)u_{x,j}u_{x,j}$ for the horizontal plane and $(\rho\Delta l)u_{z,j}u_{x,j}$ for the vertical plane.

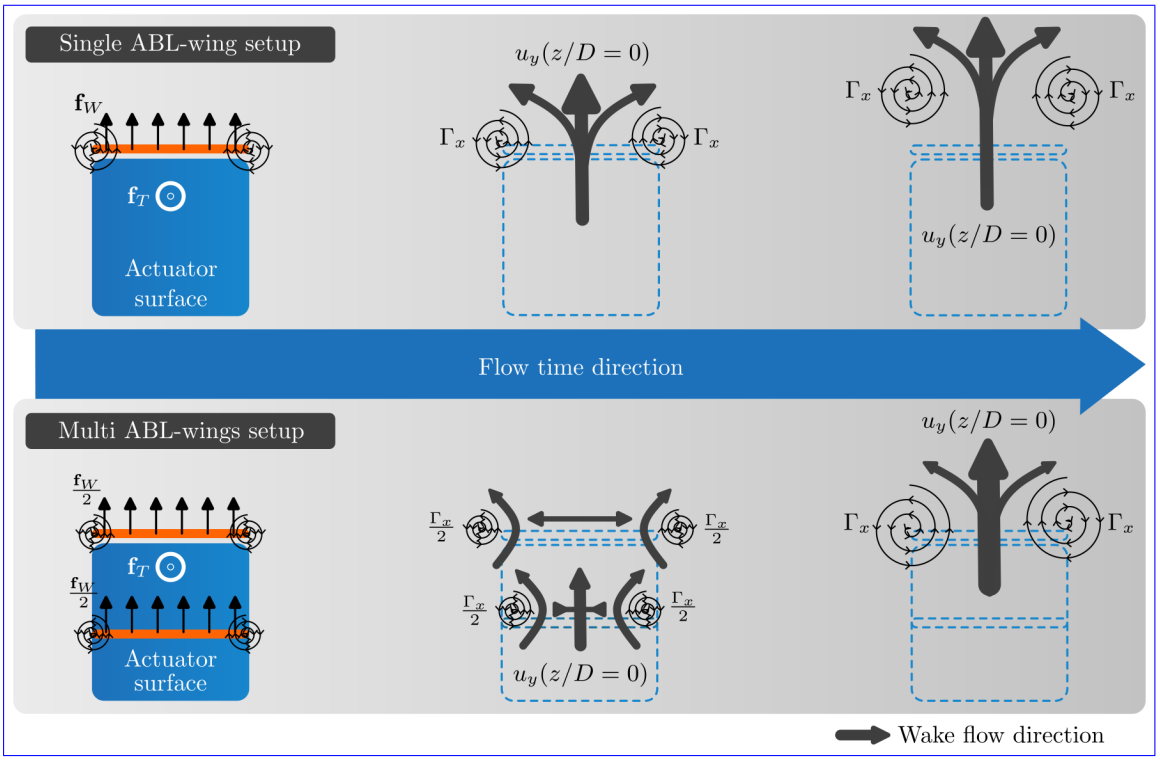


**Figure 10.** Schematic diagram illustrating the mechanisms driving upward advection in the wake. Setups with a single wing (represented by green line segments) move wing-tip vortices farther up into the atmosphere. In contrast, setups with multiple wings elevate the wing-tip vortices more slowly but more efficiently transport low-momentum flow upwards.

To evaluate the streamwise momentum exchanged between the wake flow and the surrounding fluid, we propose using the normalized velocity products $u_x u_x/U_\infty^2$ and $u_z u_x/U_\infty^2$ across the horizontal and vertical planes, respectively.

Figure 11 presents the velocity products ~~at~~ on a horizontal plane at ~~$y/D = 1.1$ to qualitatively assess the ABL-controlling effects on vertical momentum fluxand the enhancement of power extraction. Negative~~ $y/D = 1.1$, offering a qualitative assessment of the impact of ABL control on streamwise momentum flux. Positive values of the product ~~$-u_y u_x$~~ $u_y u_x$ indicate momentum transfer from below ~~to above the plane , while positive values indicate transfer from above to below the~~ the plane to above, while negative values signify the entrainment of high-momentum ABL flow into the wake, which is most prevalent at $|z/D| > 0.5$. The results shown in Fig. 11 ~~align with previous observations~~ corroborate previous findings from the velocity ~~fields in § 3.2, showing~~ field analysis discussed in Section 3.2. They confirm that all ABL-controlled ~~setups significantly increase~~ configurations significantly enhance vertical momentum exchange between the ~~ABL~~ flow above and the wake ~~. This increase is expected, given~~ flow, consistent with the higher vertical velocity ~~component observed in ABL-controlled setups.~~

~~The negative $-u_y u_x$ values in the ABL-controlled configurations suggest that low-momentum flow parcels in the wake are advected upward. Conversely, positive values indicate that high-momentum flow from the ABL is entrained into the wind-farm flow from the sides of the wake ($|z/D| > 0.5$). The $-u_y u_x$ fields also demonstrate a significant performance gain when~~

~~using~~ components observed in these setups. Furthermore, the $u_y u_x$ fields demonstrate a notable performance improvement when employing the 2- ~~or~~ and 4-wing ~~design~~ designs compared to the single-wing ~~design of~~ configuration in Case 1W. This improvement ~~arises from~~ is attributed to a more uniform distribution of circulation ~~$\Gamma_x$~~ $\Gamma_x$ across the wake~~. This uniformity~~ , which reduces the average distance between the ~~rotation center of the wing-tip vortex~~ vortex core and the low-momentum flow ~~parcels in~~ regions within the wake, thereby ~~enhancing momentum fluxes across the $y/D = 1.0$~~ increasing momentum flux across the $y/D = 1.0$ plane.

Figure 12 ~~displays the velocity products $u_z u_x$~~ shows the velocity product $u_z u_x$ from a side-plane view at ~~$z/D = 0.5$~~$z/D = 0.5$. Positive values indicate momentum transfer ~~towards the $-z$ direction~~ in the $z$-direction (out of the ~~page~~ plane), while negative values ~~indicate the opposite . In setups~~ represent momentum transfer in the opposite direction. In configurations with a single wing, such as Cases 1W and 1W-ND, momentum exchange is ~~predominant in the near wake regionand is primarily influenced~~ predominantly concentrated in the near-wake region, driven largely by the tip vortices ~~of the single ABL~~ generated by the ABL-controlling device. In ~~configurations with more wings , the~~ contrast, configurations with multiple wings exhibit a more evenly distributed momentum exchange between the wake and ~~surrounding flows is distributed among the multiple~~ the surrounding flow across the various ABL-controlling devices. The ~~$u_z u_x$ plots also reveal that regions with~~ velocity products also demonstrate that regions of positive momentum entrainment (~~brightly-coloured regions) are~~ represented by red-shifted colors) remain aligned behind the disk actuator ~~in setups with more wings~~further downstream in multi-wing setups. This suggests that ~~while configurations with more wings may not be as effective in quickly~~ although configurations with additional wings may be less effective at rapidly advecting wing-tip vortices ~~upwards~~upward, they are more efficient at ~~pushing~~ introducing high-momentum flow into the ~~wind-farm flow~~ wake from the sides.

~~The comparison of~~ Comparing the momentum fluxes between the wake and the surrounding ~~flows~~ flow for models with and without ~~the~~ induced drag from ABL-controlling wings reveals that the ~~impact~~ distribution of induced drag ~~depends on how it is distributed across the ABL-controlling system. For instance, the results in Fig.~~significantly influences the dynamics of the ABL-controlled flows. The results in Figures 11 and 12 ~~demonstrate~~ indicate that higher momentum fluxes occur when induced drag is concentrated on a single wing~~(~~, as seen in ~~Cases~~ Case 1W~~and 1W-ND). In setups with multiple wings, where the induced drag $C_{x,W}$ is distributed over a larger wake region, the induced drag has a less significant effect on the dynamics of the ABL-controlled flows.~~

~~When the~~ . For cases where induced drag is concentrated ~~at~~ on the top wing element (at ~~$y/D = 1.1$~~)$y/D = 1.1$), there are larger velocity gradients in the near-wake region~~of that wing~~. These gradients, combined with the shearing processes in the outer layers of the wake flow, ~~lead to more intense~~ result in increased vorticity production and, consequently, more vigorous turbulent mixing. In configurations with ~~more~~ multiple wings, this effect is ~~spread~~ distributed over a larger ~~region~~ portion of the wake, ~~making the impact less pronounced~~ resulting in a less pronounced impact on the wake dynamics.

~~Lastly, the~~ The efficiency of the ~~current~~ ABL-controlling strategy is ~~also assessed~~ further evaluated through the total pressure, ~~$p_t \approx p_t(x)$,~~ $p_t \approx p_t(x)$, defined as:

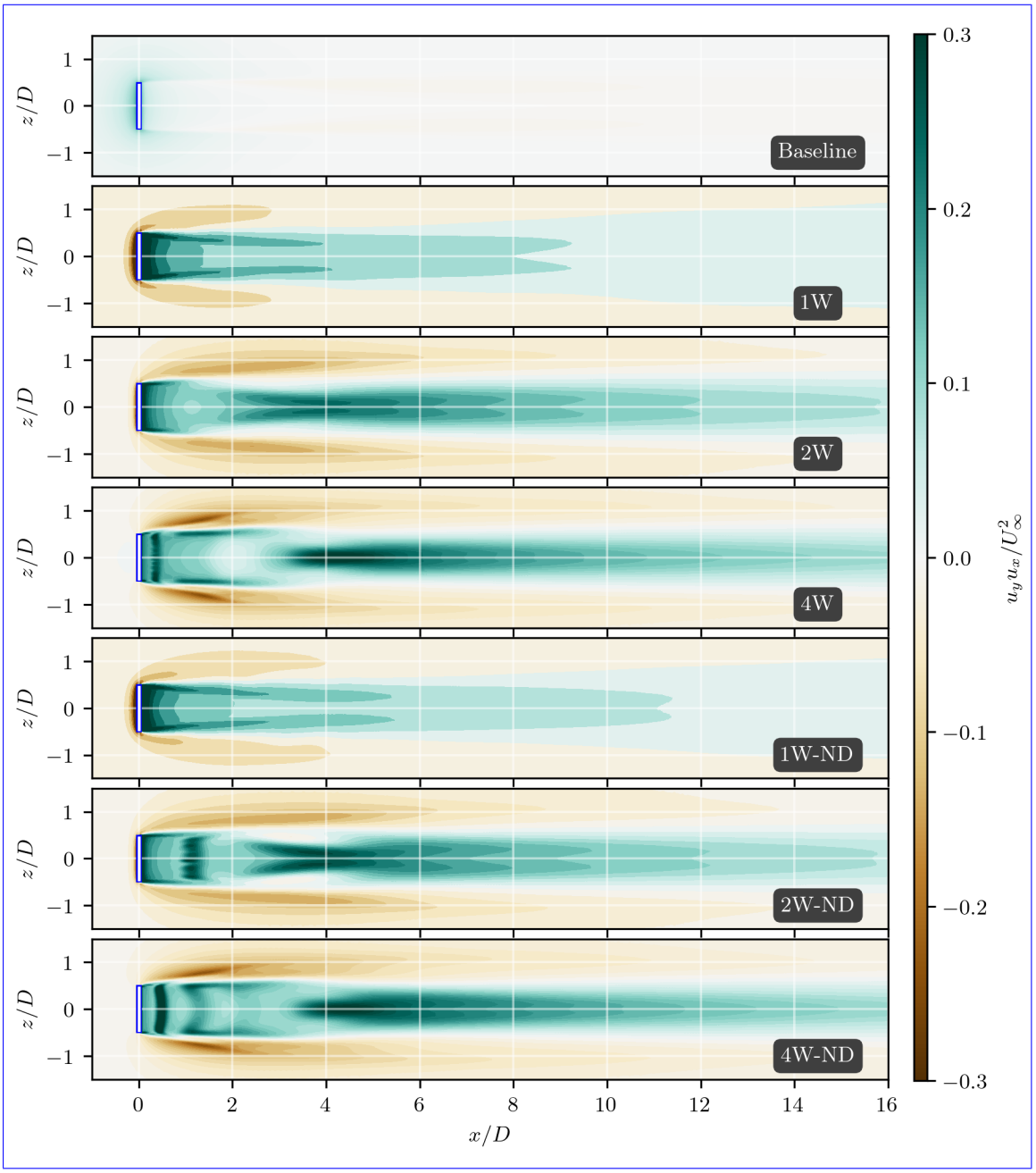


**Figure 11.** Products of vertical and streamwise velocities at the top of the disk actuator model (represented as a white box) plane, ~~$y/D = 1.1$~~ $y/D = 1.1$.

$$p_t(x) := p(x) + \frac{1}{2}\rho \sum_{i=1}^{3} \overline{\mathbf{u}}_i(x)^2 \tag{11}$$

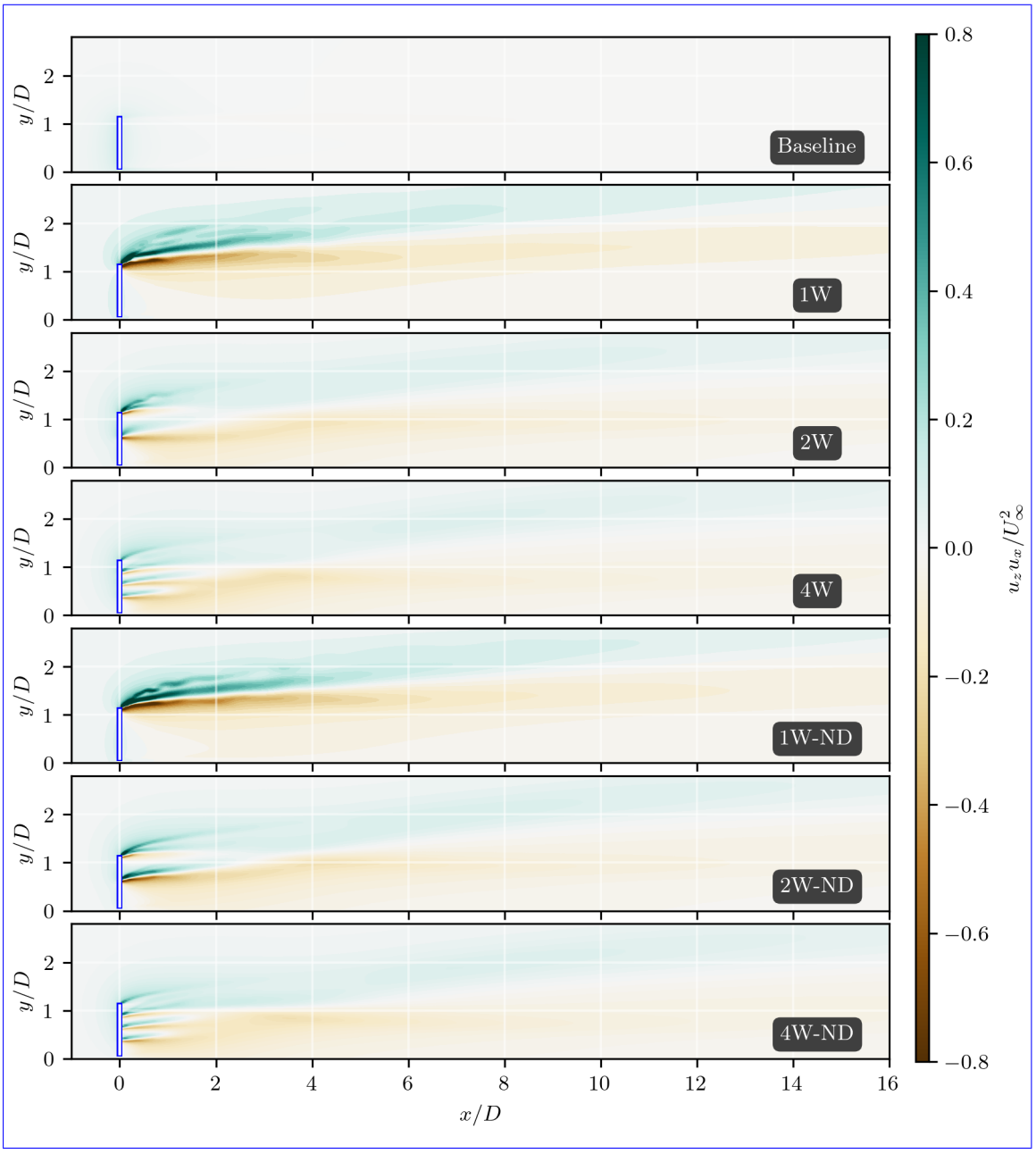


**Figure 12.** ~~Products of crosswind~~ Crosswind and streamwise ~~velocities~~ velocity products at a plane ~~at~~ on the ~~left hand~~ left-hand side of the disk actuator model (represented as a white box) ~~plane, $z/D = 0.5$~~at $z/D = 0.5$.

~~available in the wake. The~~ This total pressure is integrated ~~inside~~ within a flow volume ~~defined by~~ corresponding to the projected cross-sectional area of the actuator disk surface, ~~i.e., $\{x \in [0, +\infty[; y \in [0.1D, 1.1D]; z \in [-0.5D, 0.5D]\}$. The results for the~~

defined as $\{x \in [0, +\infty[; y \in [0.1D, 1.1D]; z \in [-0.5D, 0.5D]\}$. The variation of total pressure along the wake, ~~$p_t(x)$, are shown~~ $p_t(x)$, is presented in Fig. 13.

~~According to the Momentum~~

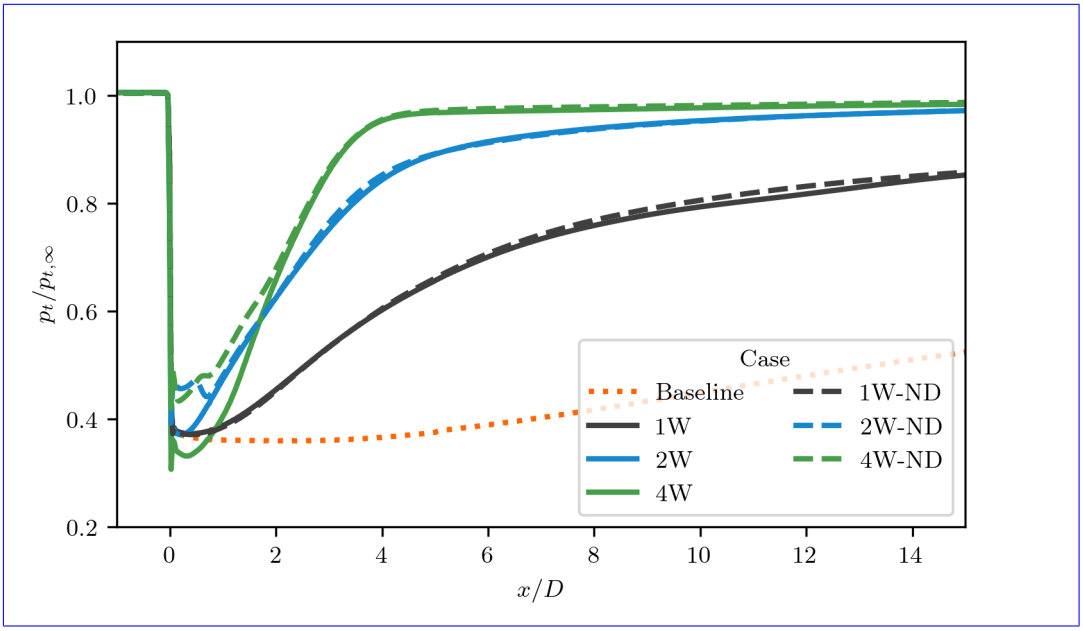


**Figure 13.** Total pressure distribution in the wake as a function of the streamwise coordinate, $x/D$, for all cases examined in this study. The total pressure is integrated within a box-shaped volume corresponding to the rotor's projected area. Dashed and solid curves represent ABL-controlled setups with and without wing-induced drag, respectively. The dotted line represents the results for the system without ABL-control.

According to momentum theory, the total pressure behind an actuator disk ~~is given by~~can be expressed as:

$$p_t(x=0) = p_\infty + \frac{1}{2}\rho\left((1-2a)U_\infty\right)^2, \tag{12}$$

where ~~$a$~~ $a$ is the induction factor, ~~$a := (U_\infty - u_x(x=0))/U_\infty$. According to the Momentum theory ,~~ $a := (U_\infty - u_x(x=0))/U_\infty$. Momentum theory further relates the induction factor ~~$a$ relates to the actuator disk's thrust coefficient $C_T$ by the equation $C_T = 4(1-a)a$~~ to the thrust coefficient $C_T$ of the actuator disk through $C_T = 4a(1-a)$. For the ~~present system , Momentum~~ system analyzed here, momentum theory predicts the total pressure in the wake to be approximately ~~$p_t/p_{t,\infty}(x/D>0) \approx 0.28$~~$p_t/p_{t,\infty}(x/D$
However, in the current viscous wake model~~can recover momentum only through velocity fluctuations around~~ , momentum recovery is driven by turbulent velocity fluctuations within the streamtube (as ~~seen~~ observed in the Baseline case). ~~When the~~ Nonetheless, when an ABL-controlling strategy is ~~applied~~implemented, wake recovery is significantly ~~faster~~ accelerated due to wake-steering, ~~and~~ making turbulent velocity fluctuations ~~become~~ a secondary mechanism for momentum entrainment and wake recovery.

Consistent with the results ~~shown~~ depicted in Figs. 11 and ~~–~~12, the total pressure integrated along the wake ~~indicates~~ demonstrates that design strategies ~~with more~~ incorporating multiple wings expedite wake recovery. ~~For instance~~Specifically, in Cases 2W ~~or~~ and 4W, the total pressure ~~in the wake~~ reaches 95% of the free-stream value at ~~$x/D \approx 5$ and 6~~approximately $x/D = 5$ and $x/D = 6$, respectively. ~~In contrast, for~~ By contrast, in the Baseline case, ~~which lacks~~ where no ABL-controlling devices are present, wake recovery is ~~substantially~~ significantly slower, and this ~~level~~ degree of recovery is not observed within the current computational domain extending to ~~$x/D = 50$~~$x/D = 50$.

~~The figure illustrates the total pressure available in the wake as a function of the streamwise flow direction, $x/D$ for all test cases in this study. The total pressure is integrated within a box-shaped volume corresponding to the rotor's projected area in the downstream direction. Dashed and solid curves represent ABL-controlled setups with and without the wing's induced drag, respectively. The dotted line illustrates the results for the system without ABL-controlling features.~~

~~The figure displays the cubed velocity for all test cases in this study. The dashed lines represent systems without induced drag from the wings, whereas the solid lines represent systems with induced drag from the wings. The dotted line illustrates the results for the system without ABL-controlling features. The thin dashed line indicates the 0.95 plateau for reference.~~

~~The analysis of the total pressureintegrated along the wake is repeated for~~ In addition to total pressure, the analysis is extended to the cubed velocity, ~~$\sum_i u_i^3(x)$. The results of this analysis are~~ $\sum_i u_i^3(x)$, shown in Fig. 14. While total pressure ~~quantifies~~ reflects the energy available ~~in~~ within the wake, the cubed velocity is a more ~~appropriate parameter for measuring~~ suitable metric for evaluating the wind power available for extraction in the ~~wind farm flow~~wake region. The cubed velocity ~~plots~~ profiles in Fig. 14 ~~reveal a significant~~ show a marked improvement in power recovery when ~~the~~ ABL-controlling ~~system is used. Comparing~~ strategies are applied. This improvement is particularly evident when comparing the Baseline case to Cases 1W and 1W-ND~~shows this enhancement clearly~~. A similar ~~improvement~~ enhancement is observed when comparing the ~~setup with two wings~~ two-wing configuration to the single-wing setup. ~~Finally, the system with four wings, which~~ Notably, the four-wing system demonstrates the fastest wake recovery among the ~~setups analyzed, recovers to~~ configurations examined, reaching 95% of the free-stream velocity at ~~$x/D = 6$~~ $x/D = 6$ downstream of the multirotor system. ~~This underscore~~ These findings highlight the potential of ~~the technology compared to current technologies without ABL-controlling devices~~ABL-control technology in comparison to current systems lacking such features.

It is important to note, however, that the present study employs a simplified numerical model to provide a proof of concept. The results presented here are not yet directly transferable to real-world scenarios. Further research is necessary to fully assess the benefits of wake recovery under atmospheric inflow conditions.

## 4 Conclusions

~~The current~~ This study introduces and evaluates a novel concept ~~of multirotor wind farm layouts, incorporating paired rotor and rotor-sized wings termed ABL-control devices , situated in the near wake~~ for regenerative wind energy, utilizing paired multirotor and multirotor-sized wings — termed Atmospheric Boundary Layer (ABL) control devices — positioned in the near-wake region. These ~~rotor-sized wings~~ ABL-control devices generate vortical structures within the ~~wind farm~~ wake flow,

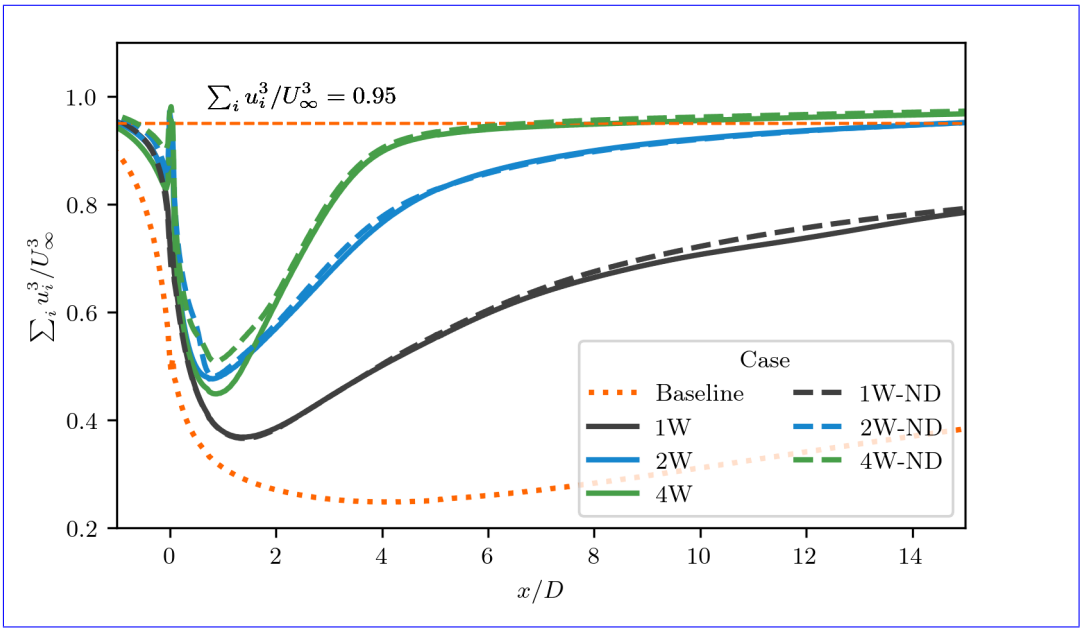


**Figure 14.** Cubed velocity for all cases examined in this study. Dashed lines represent systems without wing-induced drag, while solid lines represent systems with wing-induced drag. The dotted line corresponds to the system without ABL-control, with the dashed line indicating the 0.95 recovery plateau for reference.

enhancing the vertical momentum flux from the flow above the ~~ABL into the wind farm flow . This augmentation facilitates the wake-recovery process, leading to possible increased~~ wake flow into the wake flow region, thereby facilitating wake recovery and potentially increasing power generation per land ~~area. Multirotor and ABL-controlling devices are characterized~~ or sea area. The multirotor system and ABL-control devices are modeled using three-dimensional actuator surface models based on ~~Momentum theory. Analysis~~ momentum theory. The analysis of velocity and vorticity fields reveals that large wing-tip vortices ~~are responsible for advecting~~ advect low-momentum fluid parcels upward from the wake flow ~~upwards in exchange for moving~~ while drawing high-momentum flow from ~~the ABL downwards~~above downward. Additionally, it was observed that the induced drag of the large wings ~~comprising the ABL-controlling systems~~ within the ABL-control system could slightly enhance the mixing process at the outer shear layers of the wake~~for~~ , particularly in setups with significant and concentrated induced drag forces. ~~Hence, the current~~ These findings suggest that the induced drag ~~of the wings may favor the ABL-controlling~~ may be beneficial for the ABL-control strategy. Furthermore, the examination of momentum flux and total pressure indicates that ~~,~~ with the adoption of ~~ABL-controlling strategies, the~~ ABL-control strategies, vertical momentum flux becomes the primary mechanism for wake recovery, while velocity fluctuations ~~assume~~ play a secondary role ~~for~~ under the assessed flow conditions. ~~For~~ Notably, in the four-winged ~~ABL-controlling~~ ABL-control strategy, the total pressure and power in the wake recovered to 95% of the free-stream value at downstream positions of approximately ~~$x/D \approx 5$ and $x/D \approx 6$~~$x/D \approx 5$ and $x/D \approx 6$, respectively. These results underscore the ~~technology's potential~~ potential of this technology to reduce the land or sea area required for wind farms.

However, further research is needed to assess the effectiveness of this regenerative strategy under atmospheric inflow conditions, as the current findings are not yet directly applicable to real-world scenarios.

*Code availability.* The primary codebase which enables the multi-rotor system simulations with vortex-generating modes, is hosted on GitHub. You can access it via the following link: https://doi.org/10.5281/zenodo.11615669. This repository includes detailed documentation and example scripts to facilitate replication and extension of our work.

*Data availability.* The database presented in this study is available from the corresponding author upon reasonable request. The database is compressed in Python's Pickle library and relies on several open-source libraries, including NumPy, Pickle, SciPy, and Matplotlib.

*Author contributions.* FM: formal analysis, writing, code development. AZ: supervision and technical review. CF: funding acquisition, supervision and technical review.

*Competing interests.* The contact author has declared that none of the authors has any competing interests.

*Acknowledgements.* The authors would like to express their sincere gratitude to Thomas Broertjes for providing them with the Computer-Aided Design (CAD) model of the multirotor system. ~~EXTT~~